Monthly Notices of the ROYAL ASTRONOMICAL SOCIETY
MNRAS **552,** 1–23 (2026) https://doi.org/10.1093/mnras/stag253

ALMA Central Molecular Zone Exploration Survey (ACES) – V. CS(2 − 1), SO(2_3 − 1_2), $CH_3CHO(5_{1,4} - 4_{1,3})$, HC_3N(11 − 10) and H40α lines data

Pei-Ying Hsieh [1★] Daniel. L. Walker [2] Adam Ginsburg [3] Ashley T. Barnes [4] Xing Lu [5,6] Álvaro Sánchez-Monge [7,8] Savannah R. Gramze [3] Nazar Budaiev [3] Marc W. Pound [9] Jaime E. Pineda [10] Claire Cook,[11] Jonathan D. Henshaw [12,13] Katharina Immer [4] Namitha Issac [5] Desmond Jeff [3] Fu-Heng Liang [14,4] Steven N. Longmore [12,15] Elisabeth A. C. Mills [11] Sergio Martín [16,17] Xing Pan [18,19,20] Thushara G. S. Pillai [21] Qizhou Zhang [20] John Bally [22] Cara Battersby [23] Laura Colzi [24] Paul T. P. Ho [25] Izaskun Jiménez-Serra [24] J. M. Diederik Kruijssen [15] Maya Petkova [26] Mattia C. Sormani [27] Robin G. Tress [28] Jennifer Wallace [23] J. Armijos-Abendaño [29] Lucia Armillotta [30] N. Bijas [31] Rojita Buddhacharya [12] Laura A. Busch,[10] Natalie O. Butterfield [32] Mélanie Chevance [33,15] Ana Karla Díaz-Rodríguez [2] Christoph Federrath [34] Rubén Fedriani [35] Pablo García [36,37] Qi-Lao Gu,[5] Rebecca J. Houghton [12] Yue Hu [38] Janik Karoly [39] Ralf S. Klessen [33,40,20†] Mark R. Krumholz [34] Farideh Mazoochi [41] Francisco Nogueras-Lara [35,4] Dylan Paré [42] Denise Riquelme-Vásquez [43] Víctor M. Rivilla [24] Miriam G. Santa-Maria [3,44] Anika Schmiedeke [45] Yoshiaki Sofue [46] Volker Tolls [20] Q. Daniel Wang [47] Gwenllian M. Williams [48] Fengwei Xu [49,50] and Suinan Zhang [5]

Affiliations are listed at the end of the paper

Accepted 2026 February 2. Received 2026 February 2; in original form 2025 July 18

ABSTRACT

We present data from the ALMA Central Molecular Zone Exploration Survey (ACES) Large Program, which provides broad spectral-line and 3 mm continuum coverage of the Central Molecular Zone (CMZ) at a spatial resolution of 0.1 pc. The survey delivers homogeneous, wide-field mosaics that enable direct comparisons of the physical and chemical conditions across diverse environments in the Galactic centre. In this data release paper, we present the CS(2 − 1), SO(2_3 − 1_2), $CH_3CHO(5_{1,4} - 4_{1,3})$, HC_3N(11 − 10), and H40α lines observed simultaneously within two broad spectral windows. These lines reveal pronounced spatial and chemical variations across the CMZ, tracing distinct components of molecular gas, shock-affected regions, and ionized structures. The high angular resolution and multi-line capability of the ACES data set make it a powerful resource for future studies of gas dynamics, star formation activity, and the physical connection between the CMZ and Sgr A∗.

Key words: ISM: structure – Galaxy: centre.

1 INTRODUCTION

The Central Molecular Zone (CMZ) is a dense reservoir of molecular gas within the innermost ∼300 pc of the Galactic centre (GC), confined to a vertically thin disc with a scale height of 30–50 pc. The total gas mass is estimated at ∼ (5–10) × $10^7 M_\odot$, accounting for roughly 10 per cent of the Milky Way's molecular gas (M. Morris & E. Serabyn 1996; R. Genzel, F. Eisenhauer & S. Gillessen 2010, and references therein). Most of this mass is concentrated in compact giant molecular clouds (GMCs) with typical masses of $10^{5.5}$ to $10^{6.5} M_\odot$. Hence, the large volume of molecular gas makes it an excellent environment for star formation.

Molecular gas in the CMZ exhibits physical conditions distinct from those in the Galactic disc. The CO-to-H_2 conversion factors and gas surface densities in the CMZ resemble those found in starburst galaxies (see fig. 10 in L. J. Tacconi et al. 2008). The gas has

★ E-mail: pei-ying.hsieh@nao.ac.jp
† Elizabeth S. and Richard M. Cashin Fellow at the Radcliffe Institute for Advanced Studies at Harvard University, 10 Garden Street, Cambridge, MA 02138, USA.

© The Author(s) 2026.
Published by Oxford University Press on behalf of Royal Astronomical Society. This is an Open Access article distributed under the terms of the Creative Commons Attribution License (https://creativecommons.org/licenses/by/4.0/), which permits unrestricted reuse, distribution, and reproduction in any medium, provided the original work is properly cited.

Downloaded from academic.oup.com/mnras/article/552/2/stag253/8875762 by Liverpool John Moores University user on 02 November 2026

high temperatures, turbulence, and pressure (Y. Ao et al. 2013; E. A. C. Mills et al. 2013; A. Ginsburg et al. 2016; K. Immer et al. 2016), sharing characteristics with active star-forming regions in many different extragalactic environments (J. M. D. Kruijssen & S. N. Longmore 2013). However, despite the presence of dense gas, the current star formation rate (SFR) in the CMZ is only ∼10 per cent of what is expected from standard dense gas–SFR scaling relations (S. N. Longmore et al. 2013; A. T. Barnes et al. 2017; X. Lu et al. 2019a; J. D. Henshaw et al. 2023). Understanding how these physical conditions are related to the suppressed star formation in the CMZ requires further observational and theoretical studies which link the global gas properties to the sub-parsec scales at which star formation occurs (J. M. D. Kruijssen et al. 2014, 2019; M. R. Krumholz & J. M. D. Kruijssen 2015; M. R. Krumholz, J. M. D. Kruijssen & R. M. Crocker 2017; R. G. Tress et al. 2020; M. C. Sormani et al. 2022).

The Atacama Large Millimeter/submillimeter Array (ALMA) CMZ Exploration Survey (ACES) Large Program (S. Longmore & ACES Team 2025, project code: 2021.1.00172.L; PI: S. Longmore) provides uniform Band 3 coverage of the inner $1.5^\circ \times 0.5^\circ$ of the CMZ, producing the largest mosaic yet made with ALMA and achieving an unprecedented angular resolution of $\sim 2''$ in both spectral-line and continuum emission. This new global, high-resolution and sensitivity view of the physical, kinematic and chemical structure facilitates ACES main science objective to build a global understanding of star formation, feedback, and the mass flows and energy cycles across the Central Molecular Zone. ACES employed 6 spectral windows to span a wide range of frequency coverage. The continuum data set, covering an effective bandwidth of 4.6 GHz, is described in detail by A. Ginsburg & ACES Team (2025). The high-resolution spectral-line data and details of the data combination will be presented by D. Walker & ACES Team (2025), while the intermediate-resolution spectral-line data will be presented by X. Lu & ACES Team (2026). In this paper, we present the data release of two broadband spectral windows that include the lines of CS(2 − 1) (carbon monosulfide), SO($2_3 - 1_2$) (sulfur monoxide), $HC_3N(11 - 10)$ (cyanoacetylene), $CH_3CHO(5_{1,4} - 4_{1,3})$ (acetaldehyde), and the radio recombination line H40α. The characteristics of these lines are summarized in Table 1.

2 OBSERVATIONS AND DATA PROCESSING

Forty-five individual mosaics were used to image the central $1.5^\circ \times 0.5^\circ$ of the CMZ with the ALMA Band 3 receiver and the 12-m array. The 7-m and TP arrays were also employed to recover the short-spacing information. The overall survey design and observational setup are described in S. Longmore & ACES Team (2025, hereafter Paper I), while details of the data calibration and imaging procedures are given in A. Ginsburg & ACES Team (2025) and D. Walker & ACES Team (2025; hereafter Paper II and Paper III). The data product releases of the continuum and spectral-line cubes are presented in Paper II, Paper III, X. Lu & ACES Team (2026; Paper IV), and in this work.

We use the CASA package (CASA Team et al. 2022) for calibration and imaging. The majority of the data were processed with CASA version 6.2.1.7 and version 6.4.1.12 for the later data set, as the project extended across different observing cycles and pipeline version releases. The full details of the CASA versions used can be found in Paper II. In this paper we present the spectral cubes of the broad spectral windows (SPW 33 and SPW 35 in Table 1 of Paper III). The spectrum of broad spectral window towards the water maser core of the Brick cloud is shown in Fig. 1. The conversion factors from Jy beam^{-1} to K are 21.2, 20.7, 23.4, and 20.8 for CS(2 − 1), SO($2_3 - 1_2$), $HC_3N(11 - 10)$ and $CH_3CHO(5_{1,4} - 4_{1,3})$, respectively. Detailed descriptions of the data issues, continuum subtraction, deconvolution (image reconstruction), array combination, and mosaic procedures are provided in Paper III and in the `merge_tclean_commands.py` script in the ACES GitHub repository.[1]

The CASA task `feather` was used to combine the images from the 12 m, 7 m, and TP arrays for the data release. Section 3.5 of Paper III provides a detailed discussion of various array combination methods using CASA. In this work, we adopted the 'feather-only' approach as described in section 3.5.3 of Paper III. Additionally, X. Lu (in preparation) discussed alternative combination methods using Miriad (R. J. Sault, P. J. Teuben & M. C. H. Wright 1995). The native channel width of the broad spectral window is 1.48 km s^{-1} with an effective bandwidth of ∼ 1.86 GHz (∼ 5680 km s^{-1}). The image rms noise per 1.48 km s^{-1} channel is not uniform across the mosaics, but varies between regions typically in the range of 3–5 mJy beam^{-1}. The cube statistics are shown in Table C1. The id of each field can also be found in Paper III and Paper II. For the purpose of mosaic, image cubes of individual fields were smoothed to a common beam to produce the final, full-CMZ mosaics. The common beam size is applied to the mosaic maps, while most of the individual fields have high angular resolution, the final beam is compromised with the lowest resolution of field am. The common beam sizes of the SPW 33 and SPW 35 are $2.84'' \times 2.11''$ (position angle $= -89.46^\circ$) and $2.65'' \times 1.97''$ (position angle $= -89.96^\circ$), respectively.

We compare the ACES CS(2 − 1) data with the NRO 45 m CS(2 − 1) data (P.-Y. Hsieh et al. 2016). The spatial and spectral resolutions of the 45 m data are 38″ and 2.5 km s^{-1}, respectively. The total bandwidth of the 45 m data is 400 km s^{-1}, which is narrower than that of the ACES data. The 45 m image was obtained in units of T_A^*, and we converted it to T_B by dividing by the main-beam efficiency of 0.43 (P.-Y. Hsieh et al. 2016). To compare with the ACES map, we generated `mom0` maps for both data sets using the same method described in Section 3.1, integrating over the same velocity range and smoothing to a common beam size of 38″. The ratio image is shown in Fig. 2. The mean ratio across the masked region is approximately 0.9, indicating that our flux calibration is consistent with the 45 m data. Elevated ratios near Sgr C may be affected by edge effects in the maps, while the high values near Sgr A∗ are likely due to residual continuum emission in the ACES data.

3 ACES DATA PRODUCTS AND STRUCTURAL HIGHLIGHTS

3.1 Moment maps of CMZ mosaics

We present the integrated intensity (`mom0`) and peak intensity (`mom8` mosaic images (a nomenclature within the immoments task of CASA) of these four molecular lines in Figs 3, 4, and 5. The zoomed-in images of H40α are presented in Fig. A1.

[1] https://github.com/ACES-CMZ/reduction_ACES

Downloaded from academic.oup.com/mnras/article/552/2/stag253/8875762 by Liverpool John Moores University user on 02 November 2026

Table 1. Key lines covered by the broadband spectral windows.

Lines	Rest frequency (GHz)	A_{ul} s^{-1}	E_u/k (K)	n_{crit}[a] (cm^{-3})
CS(2 − 1)	97.98095	1.679E-5	7.1	2.8×10^5
SO(2_3 − 1_2)	99.29987	1.125E-5	9.2	2.9×10^5
$CH_3CHO(5_{1,4} - 4_{1,3})$ E	98.86331	3.104E-5	16.6	1×10^6
$CH_3CHO(5_{1,4} - 4_{1,3})$ A	98.90095	3.108E-5	16.5	1×10^6
$HC_3N(11 - 10)$	100.07639	0.777E-4	28.8	1.5×10^6
H40α	99.02295	–	–	–

Note.[a] Calculated assuming a gas temperature of 100 K. Critical densities are calculated as $n_{crit} = A_{ul}/\gamma_{ul}$, where A_{ul} is the Einstein coefficient and γ_{ul} is the collisional rate. The values at 100 K are taken from the Leiden Atomic and Molecular Database (F. L. Schöier et al. 2005) and the JPL spectroscopic database (H. M. Pickett et al. 1998). As no collisional rate is available for $CH_3CHO(5_{1,4} - 4_{1,3})$, its critical density is estimated using the collisional rate of CH_3OH as a close approximation.

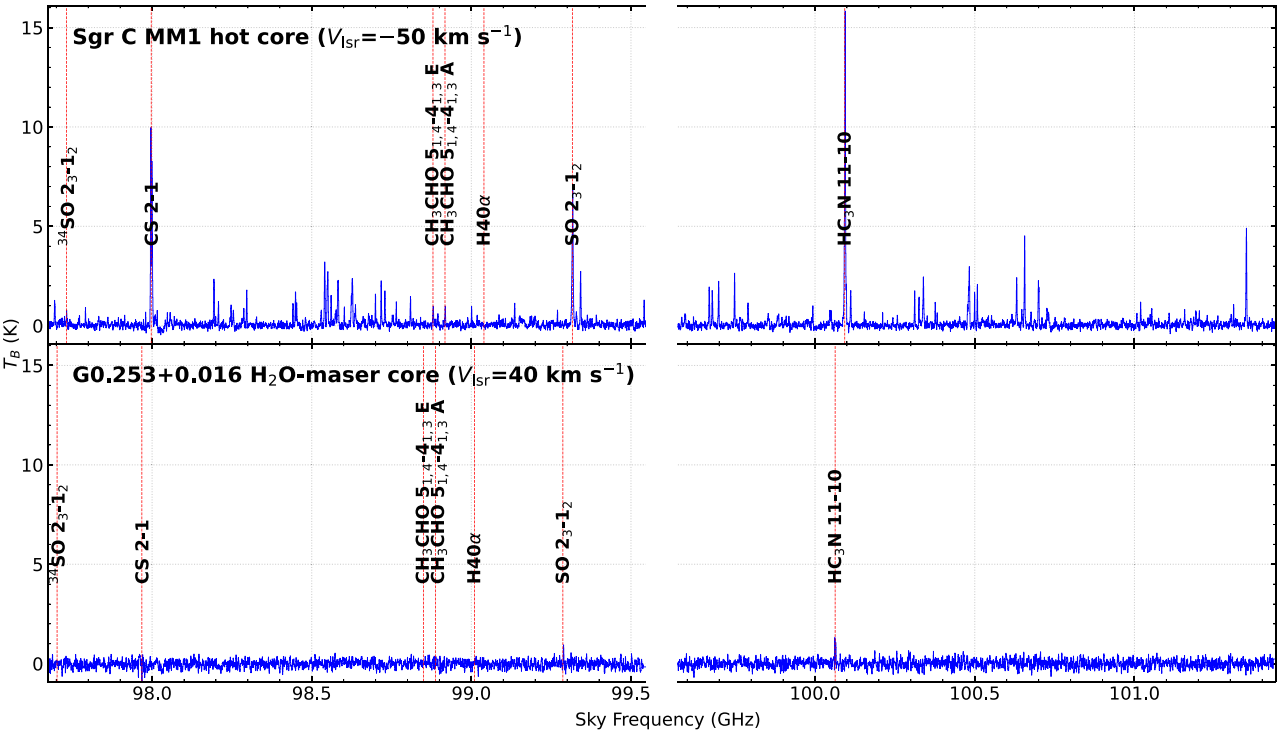


Figure 1. The spectra of broad spectral windows (SPW 33, 35) towards the Sgr C MM1 hot core and water maser core of Brick cloud. The lines presented in this paper are labelled. The native channel width of broad spectral window is 1.48 km s^{-1} with an effective bandwidth of ∼ 1.86 GHz (∼ 5680 km s^{-1} per spectral window).

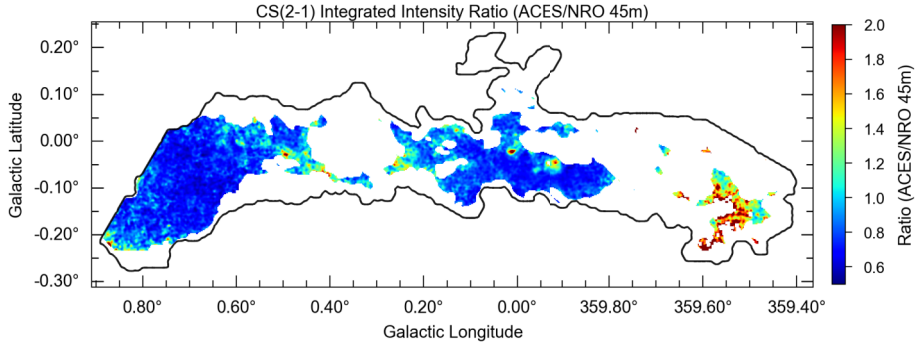


Figure 2. The ratio of ACES and NRO 45m map. The ratio map was made with the integrated intensity maps.

Downloaded from academic.oup.com/mnras/article/552/2/stag253/8875762 by Liverpool John Moores University user on 02 November 2026

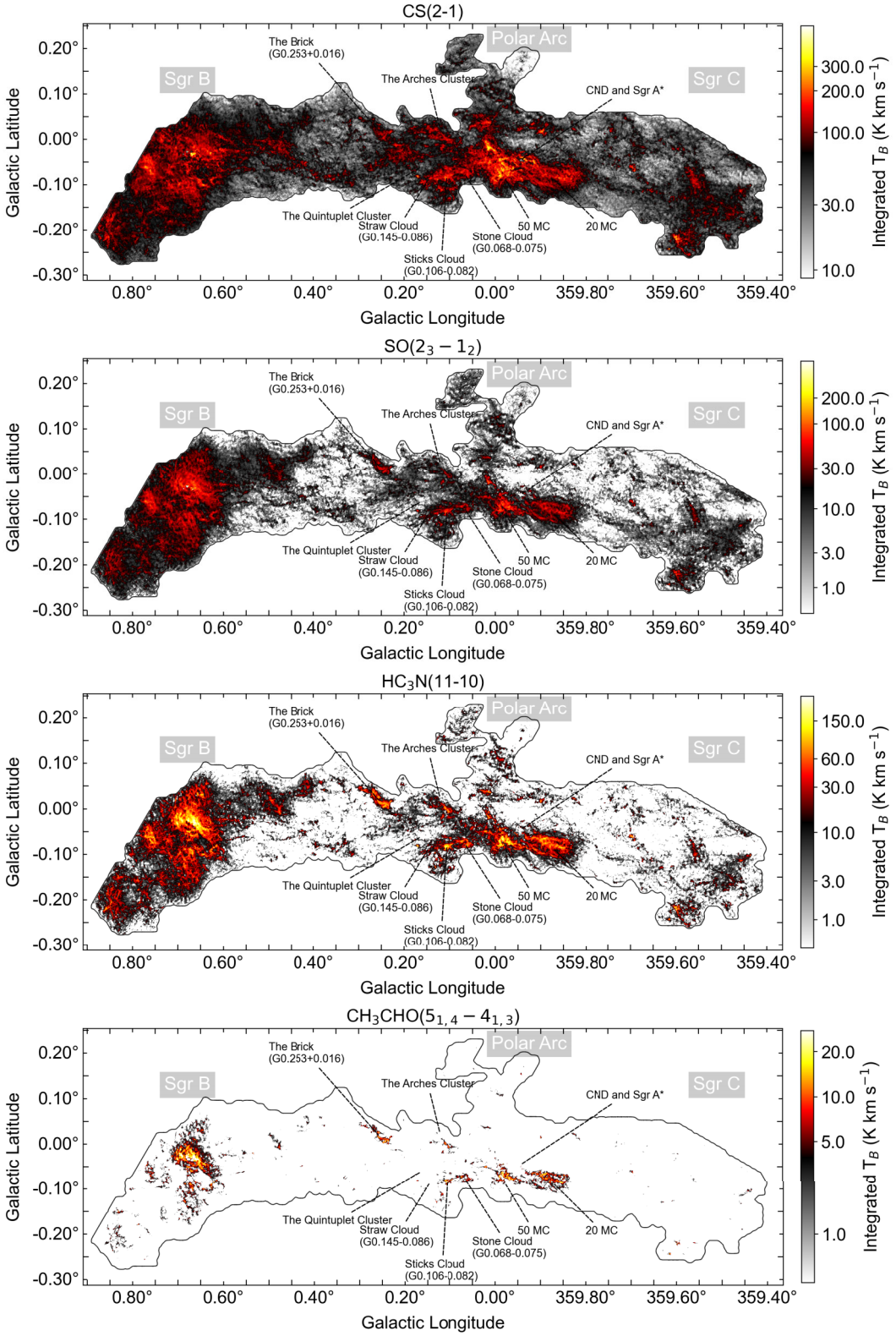


Figure 3. ALMA integrated intensity maps (`mom 0`) of CS($2-1$), SO($2_3 - 1_2$), HC$_3$N($11-10$) and CH$_3$CHO($5_{1,4} - 4_{1,3}$) lines towards the CMZ. The nomenclature of previously identified features is labelled. The common beam size is $2.84'' \times 2.11''$ with a position angle of -89.46° for the CS($2-1$), SO($2_3 - 1_2$), and CH$_3$CHO($5_{1,4} - 4_{1,3}$) lines. The common beam size is $2.65'' \times 1.97''$ with a position angle of -89.96° for the HC$_3$N($11-10$) line. Note that the acetaldehyde line (CH$_3$CHO($5_{1,4} - 4_{1,3}$)) maps are integrated with CH$_3$CHO($5_{1,4} - 4_{1,3}$) E and CH$_3$CHO($5_{1,4} - 4_{1,3}$) A.

Downloaded from academic.oup.com/mnras/article/552/2/stag253/8875762 by Liverpool John Moores University user on 02 November 2026

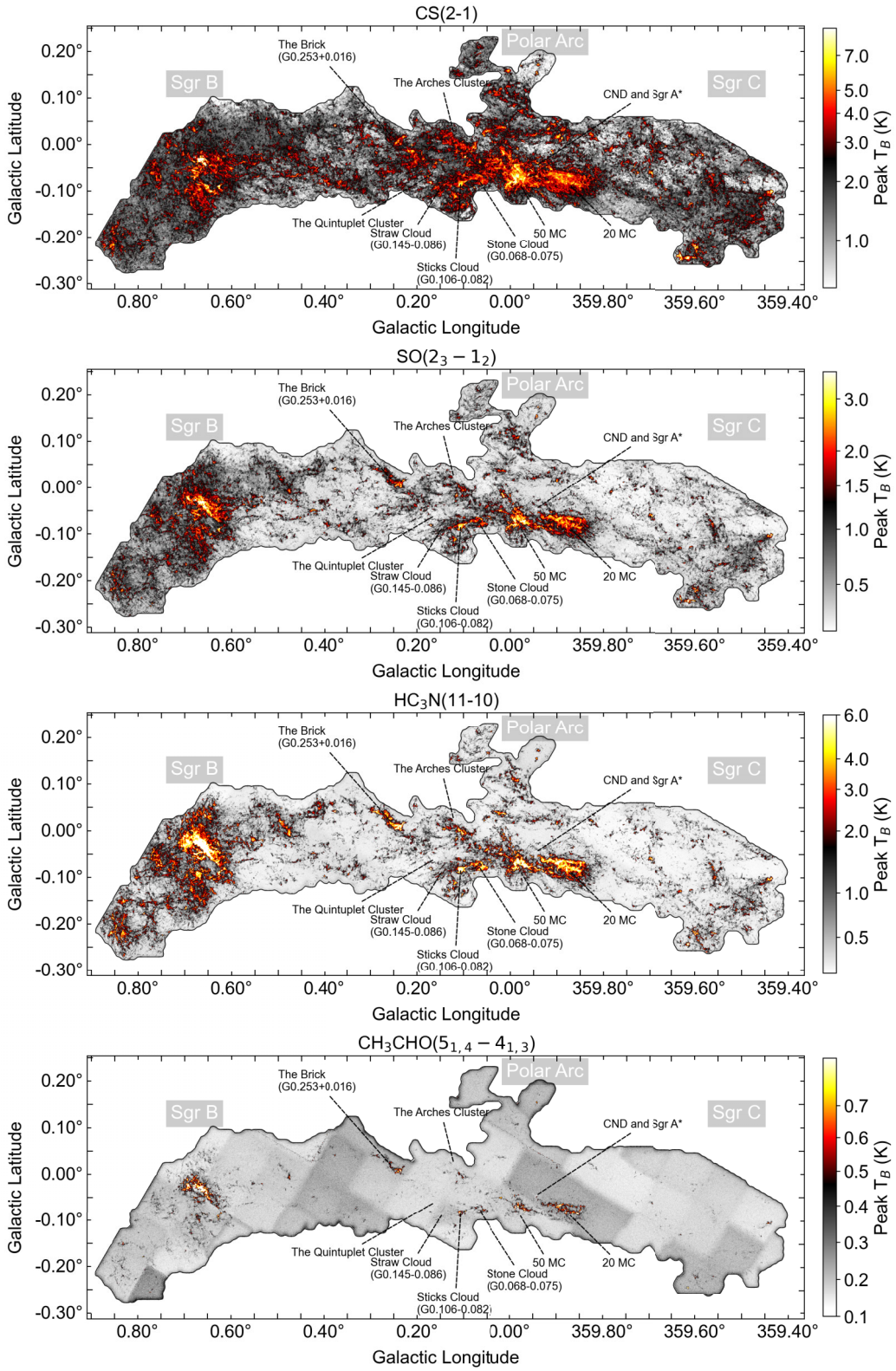


Figure 4. ALMA peak intensity maps (`mom 8`) of CS(2 − 1), SO(2$_3$ − 1$_2$), HC$_3$N(11 − 10) and CH$_3$CHO(5$_{1,4}$ − 4$_{1,3}$) lines towards the CMZ. Note that the acetaldehyde line (CH$_3$CHO(5$_{1,4}$ − 4$_{1,3}$)) maps are stacked with CH$_3$CHO(5$_{1,4}$ − 4$_{1,3}$) E and CH$_3$CHO(5$_{1,4}$ − 4$_{1,3}$) A (also see Fig. 1).

Note that the CH$_3$CHO(5$_{1,4}$ − 4$_{1,3}$) `mom0` map includes both the CH$_3$CHO(5$_{1,4}$ − 4$_{1,3}$) E and CH$_3$CHO(5$_{1,4}$ − 4$_{1,3}$) A transitions to improve the signal-to-noise ratio. These two lines are close in frequency, separated by approximately ±150 km s^{-1}. If high-velocity components (e.g. ±150 km s^{-1}), such as those from the circumnuclear disc (CND) are present, the lines may

Downloaded from academic.oup.com/mnras/article/552/2/stag253/8875762 by Liverpool John Moores University user on 02 November 2026

become spectrally blended in our data. However, since the CND is not clearly detected in either transition, the $CH_3CHO(5_{1,4} - 4_{1,3})$ `mom0` map shown in Fig. 3 is not affected by blending from high-velocity components. Users can generate individual `mom0` maps for each transition directly from the mosaic cube. Details on generating moment maps can be found in Paper III.

The moment maps provide a detailed view of the spatial distribution of emission across the CMZ. In general the ALMA maps show a combination of extended emission and compact features. The $SO(2_3 - 1_2)$ and $CS(2 - 1)$ maps reveal a smooth and diffuse emission structure, highlighting extended regions of molecular gas across the CMZ. In contrast, the $CH_3CHO(5_{1,4} - 4_{1,3})$ map is more concentrated towards the Brick, the 20 km s^{-1} cloud, the 50 km s^{-1} cloud, and the Sgr B region. The $HC_3N(11 - 10)$ emission exhibits an intermediate morphology, sharing characteristics of both the extended $SO(2_3 - 1_2)$ and $CS(2 - 1)$ emission and the compact $CH_3CHO(5_{1,4} - 4_{1,3})$ structures. The H40α map displays distinct, compact emission structures that are characteristic of ionized gas. A zoomed-in view of the H40α map with significant detection is shown in Fig. A1. Together, these maps provide a multi-line view of the gas properties, distinguishing between ionized and molecular components, and reveal the physical and chemical conditions of the observed region. However, since the molecular lines ($CS(2 - 1)$, $CH_3CHO(5_{1,4} - 4_{1,3})$, $SO(2_3 - 1_2)$, and $HC_3N(11 - 10)$) primarily trace molecular gas that is spatially anti-correlated with the ionized gas traced by H40α (cf. Fig. B1), a comparison between the H40α emission and the continuum is more physically relevant. Therefore, we do not discuss the H40α properties in detail in this paper. Readers are referred to A. Ginsburg & ACES Team (2025) for a detailed description of the continuum emission. Although that work does not discuss the H40α line, a direct comparison with the maps presented here may help to examine the spatial relation between ionized and molecular components.

The characteristic kinetic temperature in the CMZ has been reported as 65±10 K by Y. Ao et al. (2013) and within the range of 50-100 K (A. Ginsburg et al. 2016; N. Krieger et al. 2017). As shown in Fig. 4, $CS(2 - 1)$ exhibits a peak brightness temperature of approximately 10 K, particularly towards the Sgr A and Sgr B regions. This relatively high brightness temperature, comparable to the typical kinetic temperature in the CMZ, suggests that $CS(2 - 1)$ emission is generally optically thick or moderately thick, tracing gas with significant optical depth across most regions.

In contrast, $SO(2_3 - 1_2)$ and $HC_3N(11 - 10)$ show peak brightness temperatures of about 4-6 K. Although lower than that of $CS(2 - 1)$, these values indicate that the lines are moderately optically thin to moderately thick, likely reflecting somewhat lower column densities or smaller beam filling factors compared to $CS(2 - 1)$.

Meanwhile, $CH_3CHO(5_{1,4} - 4_{1,3})$ shows a peak brightness temperature of $\leq$1 K, indicating that its emission might be optically thin across most of the mapped region, similar to the $HC^{15}N$ line reported in X. Lu (in preparation). With additional SO transitions available in the ACES data (Paper I), including the isotopologue line ^{34}SO (2_3-1_2), which is expected to be optically thin, as well as SO (2_2-1_1) and SO (5_4-4_4), future studies can derive detailed temperature and density distributions to better characterize the excitation conditions in various regions of the CMZ.

3.2 `mom 1` map and longitude–velocity maps

In Fig. 6, we present the `mom 1` images of four molecular lines of the CMZ. The `mom 1` map of H40α is shown separately in Fig. 5. Despite being derived from high-resolution ALMA data, the velocity fields reveal large-scale coherent rotation, with redshifted emission at positive longitudes and blueshifted emission at negative longitudes, consistent with previous single-dish observations (e.g. P. A. Jones et al. 2012). On smaller scales, several regions show overlapping red- and blueshifted components, indicative of multiple gas streamers or distinct kinematic features along the line of sight (e.g. J. D. Henshaw et al. 2016; D. Lipman et al. 2025; D. L. Walker et al. 2025).

In Fig. 7, we present the longitude–velocity (l-v) diagrams of the four molecular lines showing intensity peaks. In the $CS(2 - 1)$ line, the horizontal absorption features at −52, −28, and −3 km s^{-1} are due to foreground absorption, which is attributed to gas in spiral arms along the line of sight at these velocities (P. A. Jones et al. 2012). The same features can be seen in other abundant molecules such as HCO^+ (Paper III). However, these foreground absorption features are not found in the other lines presented in this paper.

These complex motions associated with sub-pc scale filaments and broad-linewidth clumps observed in the velocity map are more clearly revealed in the l-v diagrams. Towards the Sgr A complex region, in Fig. 8, we present the l-v diagram of the CND. The streamers are shown as in the previous work by P.-Y. Hsieh et al. (2017). The high-velocity gas standing out from the CMZ ring (associated with the 50 and 20 km s^{-1} clouds in this figure) represents the CND and the streamers, which are kinematically distinct in both velocity structure and spatial location. These features also exhibit significantly broader linewidths ($\geq$ 30 km s^{-1}) compared to the surrounding CMZ gas, further highlighting their dynamic nature associated with tidal disruption in the deep potential well. The high spectral and spatial resolution mosaic map will enable study the infall of gas further out.

In comparison to the l-v diagrams in P. A. Jones et al. (2012) at 39″ resolution, while the Mopra data successfully traces the large-scale spiral arm structure and provides a comprehensive view of the galactic-scale kinematics across the CMZ at sub-pc scale. The low spatial resolution limits the study of motion of gas connected the CMZ and the CND. The broad linewidth clumps present in several places of the CMZ are also marginally resolved in the Mopra data. The broad linewidth clumps characteristic of the turbulent and shocked gas in this environment, leaving the physical origin and role of these velocity components unclear. ALMA data represent a crucial intermediate scale that bridges the gap between the large-scale dynamics captured by single-dish surveys and the sub-pc clumps, showing the necessity of high angular resolution observations to fully characterize the complex interplay between inflow, turbulence, and star formation in GC environments.

3.3 Key structures

In Figs 8, 9, 10, 11, and 12, we show zoomed-in images of the four molecular lines towards the well-known features interesting for star formation in the CMZ, namely, the CND, the Brick cloud, the 20 and 50 km s^{-1} clouds, and the Three Little Pigs (Sticks, Straw, and Stone clouds).

Downloaded from academic.oup.com/mnras/article/552/2/stag253/8875762 by Liverpool John Moores University user on 02 November 2026

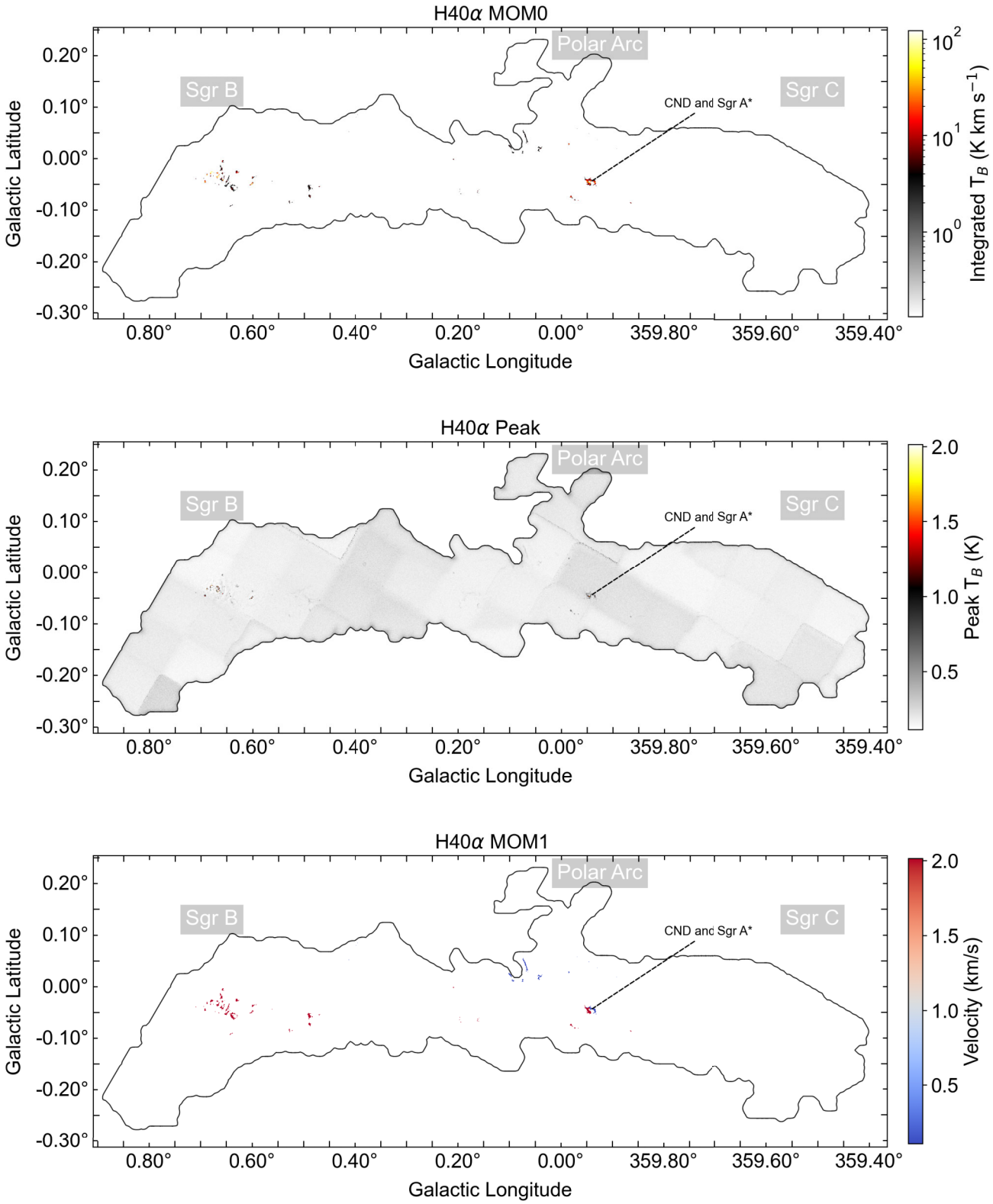


Figure 5. ALMA mosaic map of H40α line towards the CMZ. From the top to the bottom we present the `mom 0`, peak intensity, and `mom 1` images. The common beam size is $2.84'' \times 2.11''$ with a position angle of -89.46°.

Downloaded from academic.oup.com/mnras/article/552/2/stag253/8875762 by Liverpool John Moores University user on 02 November 2026

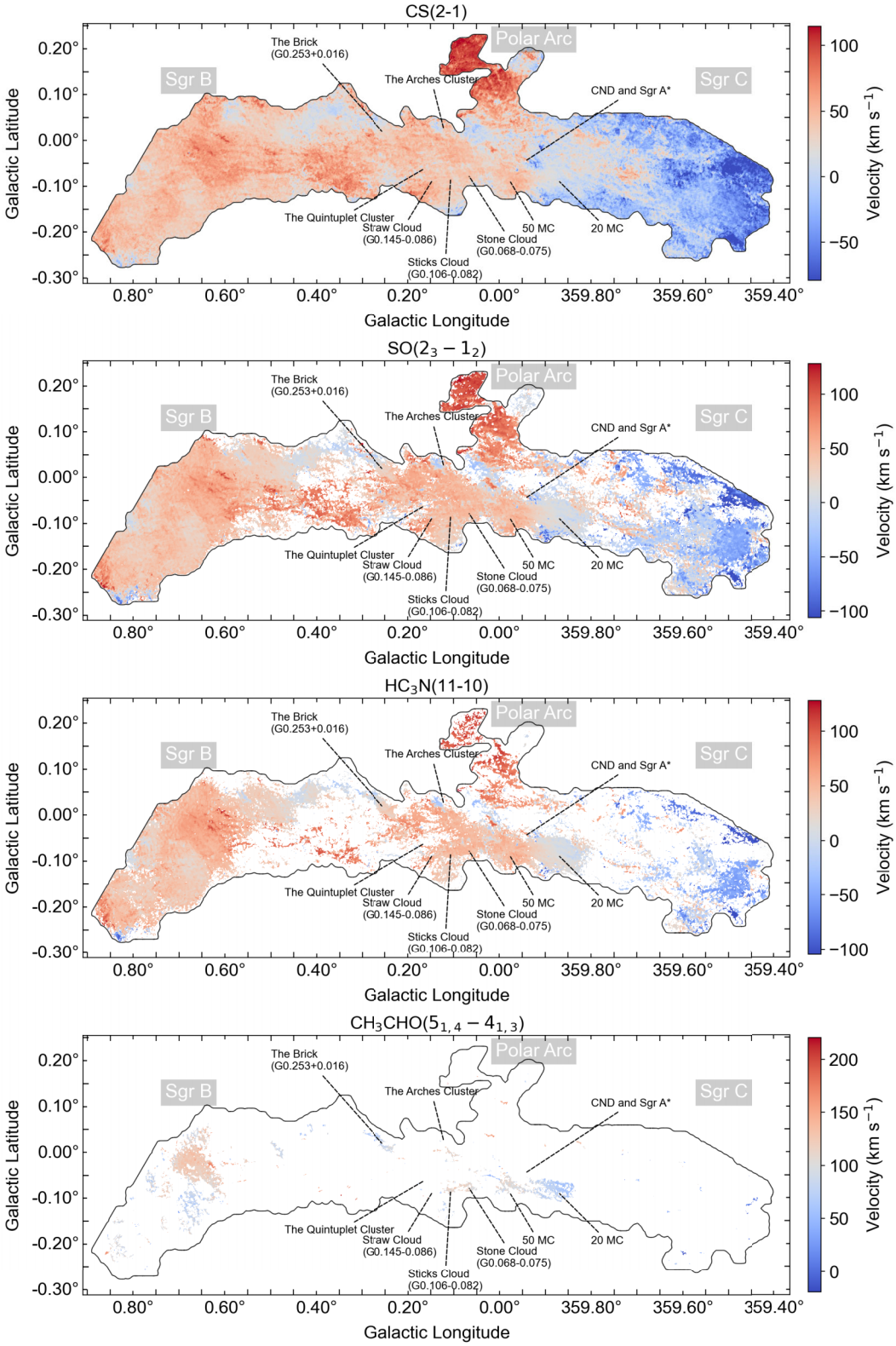


Figure 6. The intensity weighted velocity map (`mom 1`) of CS(2 − 1), SO(2$_3$ − 1$_2$), HC$_3$N(11 − 10) and CH$_3$CHO(5$_{1,4}$ − 4$_{1,3}$) lines towards the CMZ.

3.3.1 The circumnuclear disc

The circumnuclear disc (CND) is a molecular ring rotating around Sgr A∗. It contains a molecular gas mass of approximately 10^4 M$_\odot$ (e.g. M. A. Requena-Torres et al. 2012; E. A. C. Mills et al. 2013; P.-Y. Hsieh et al. 2021) and with a radius of ∼2 pc. Within this region lie the ionized streamers known as the mini-spiral (or Sgr A West; J.-H. Zhao et al. 2009) (Fig. A1 in

Downloaded from academic.oup.com/mnras/article/552/2/stag253/8875762 by Liverpool John Moores University user on 02 November 2026

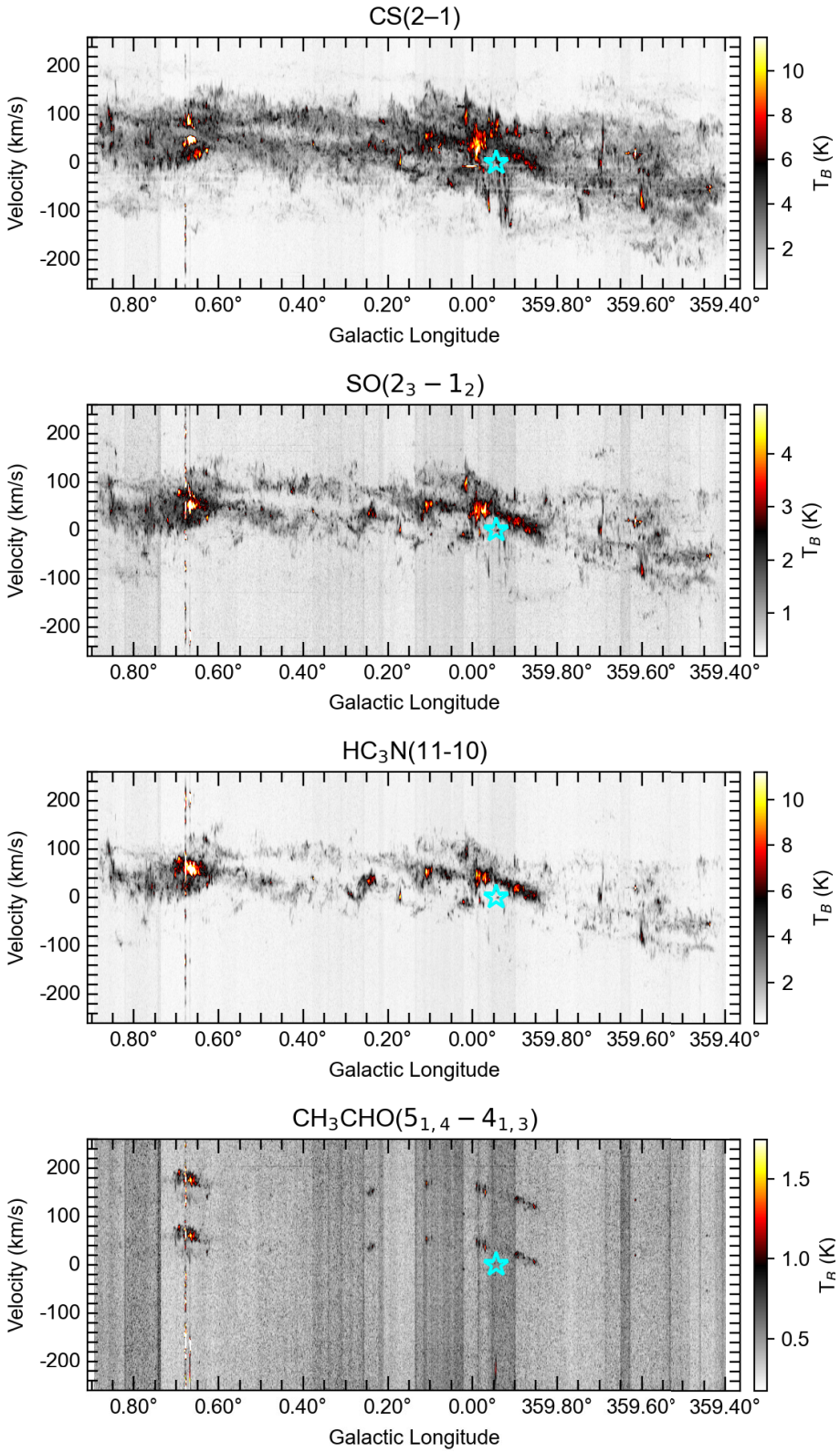


Figure 7. The longitude–velocity diagram of CS(2 − 1), $SO(2_3 - 1_2)$, $HC_3N(11 - 10)$ and $CH_3CHO(5_{1,4} - 4_{1,3})$ lines towards the CMZ. The location of Sgr A∗ is labelled with the star marker. The $CH_3CHO(5_{1,4} - 4_{1,3})$ E ($f_{\rm rest}$ = 98.86331 GHz). and $CH_3CHO(5_{1,4} - 4_{1,3})$ A ($f_{\rm rest}$ = 98.9005 GHz) can be seen together in the diagram, where we set the rest frequency of $CH_3CHO(5_{1,4} - 4_{1,3})$ A.

Downloaded from academic.oup.com/mnras/article/552/2/stag253/8875762 by Liverpool John Moores University user on 02 November 2026

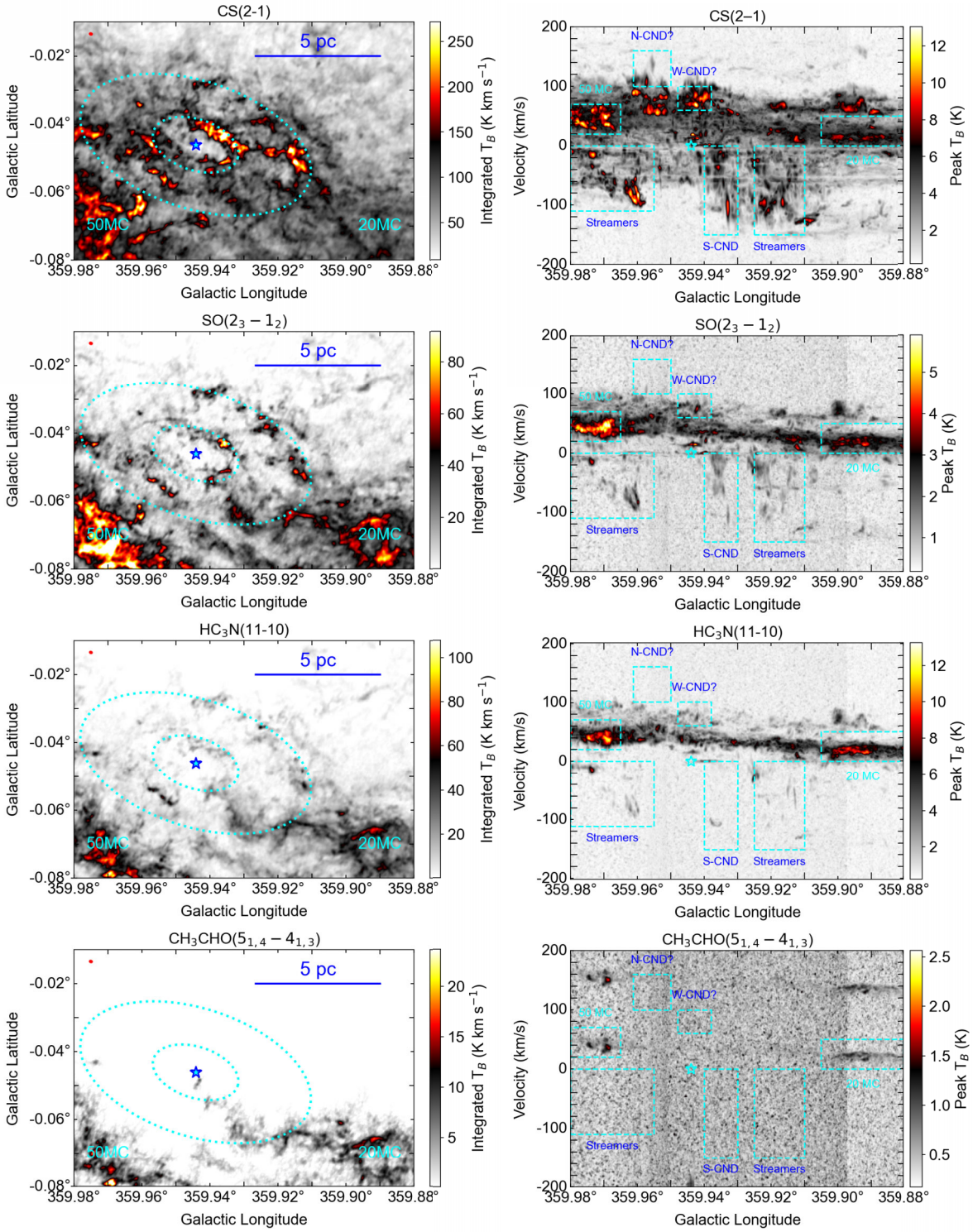


Figure 8. Left: the `mom 0` image of the CND. Sgr A∗ is marked with a star marker, and the CND is outlined with a small dotted ellipse. The streamers are outlined with the big ellipse (H. B. Liu et al. 2013; P.-Y. Hsieh et al. 2017). The CS(2 − 1), SO($2_3 - 1_2$), $HC_3N(11-10)$ and $CH_3CHO(5_{1,4} - 4_{1,3})$ lines images are presented. The beam is shown in the top left corner as a filled eliipse. Right: the longitude–velocity diagrams of the four molecular lines zoomed-in to the region of the CND.

this paper) and the nuclear star cluster (D. F. Figer et al. 1999). The streamers surrounding the CND are thought to be tidally stretched gas originating from nearby clouds (the 50 and 20 km s^{-1} clouds) that is accreting onto the CND. As the most massive and closest molecular reservoir to Sgr A∗, the CND is of great interest for understanding both the fueling of the central black hole and nuclear star formation. The ACES high-resolution mosaic of the nuclear region enables studies of gas inflow kinematics and

Downloaded from academic.oup.com/mnras/article/552/2/stag253/8875762 by Liverpool John Moores University user on 02 November 2026

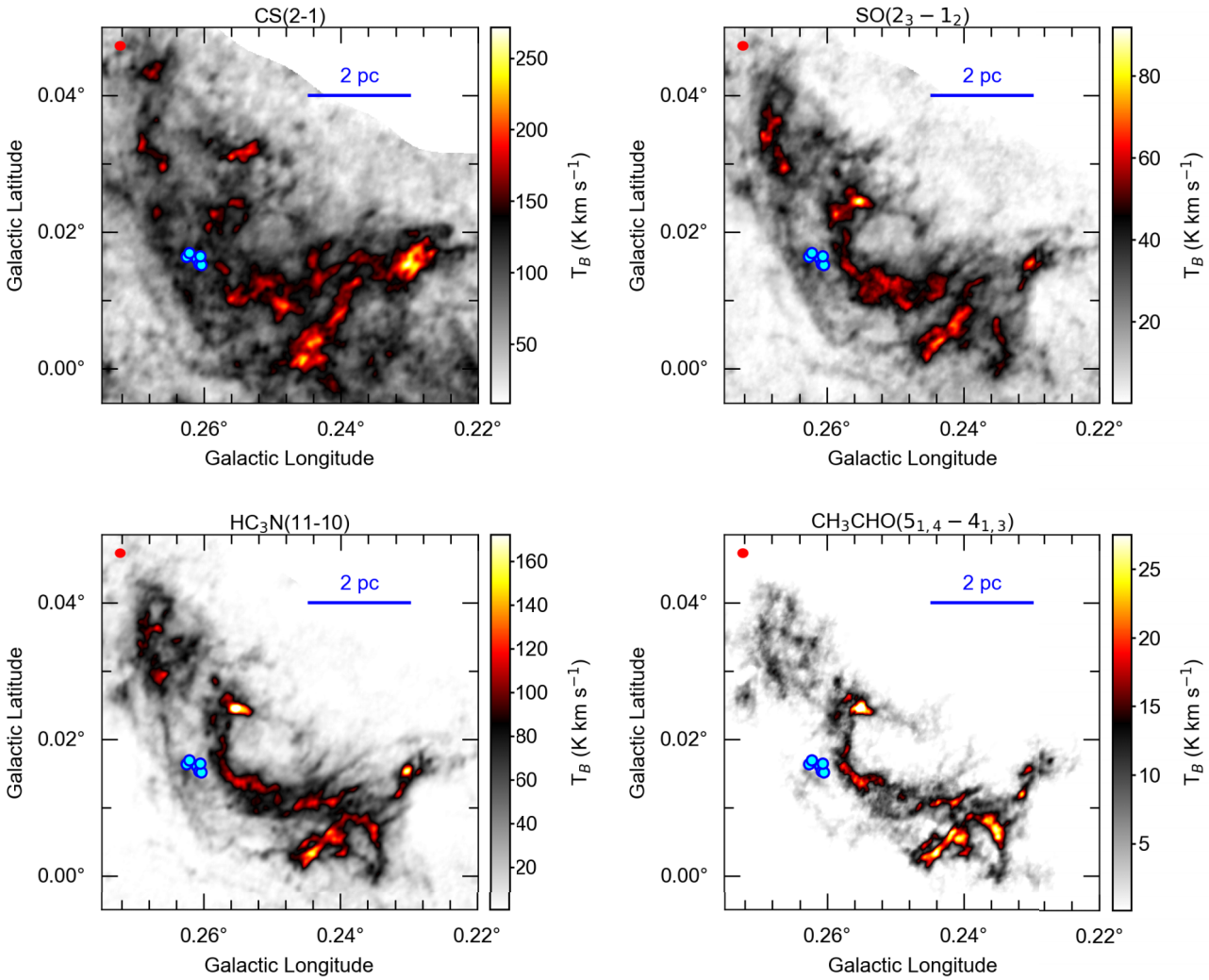


Figure 9. The `mom 0` images of the Brick cloud (G0.253 + 0.016). The CS(2 − 1), SO(2_3 − 1_2), HC_3N(11 − 10) and $CH_3CHO(5_{1,4} - 4_{1,3})$ line images are presented. The outflow positions featuring ongoing star formation are labelled with the cyan circles (D. L. Walker et al. 2021). The synthesized beam is shown in the top left corner with a red ellipse.

chemical conditions from the CMZ to the CND (e.g. Y. Sofue et al. 2025).

In Fig. 8, the CND and the streamers (H. B. Liu et al. 2013; P.-Y. Hsieh et al. 2017, 2021) are outlined with small and large cyan dotted ellipses, respectively. Both the CND and the streamers are detected in the CS(2 − 1), SO(2_3 − 1_2), and faint emission with HC_3N(11 − 10) lines; however, only the streamers visually connecting to the 20 km s^{-1} cloud are detected in the $CH_3CHO(5_{1,4} - 4_{1,3})$ line.

In the vicinity of the nuclear star cluster and Sgr A∗, UV fields can photodissociate and deplete HC_3N, although the molecule may still survive in dense, well-shielded clumps (A. Rodriguez-Franco, J. Martin-Pintado & A. Fuente 1998; D. S. Meier & J. L. Turner 2005; S. Martín et al. 2012; N. Harada et al. 2015; J. E. Lindberg et al. 2011). The weak HC_3N(11 − 10) emission in the ACES map could therefore arise from a combination of UV photodissociation and excitation effects, as the warm gas in the CND may preferentially populate higher-*J* transitions. To quantify the relative effect of UV shielding and excitation, future observations of high-excitation HC_3N lines and detailed abundance analyses will be required, which we leave for community follow-up.

3.3.2 The brick

G0.253 + 0.016, an infrared dark cloud known as 'the Brick', is one of the most massive and dense molecular clouds in the CMZ. It has a low dust temperature of 20 K, a n_{H_2} of $\geq 10^4$ cm^{-3}, and a large gas mass of $\geq 10^5$ $M_\odot$ within size of 2–3 pc. It is considered an ideal site for forming high-mass stars (D. C. Lis & J. E. Carlstrom 1994; D. C. Lis et al. 2001). Despite having the right conditions for star formation, it shows little to no star formation activity (e.g. K. Immer et al. 2012; J. Kauffmann, T. Pillai & Q. Zhang 2013; J. M. Rathborne et al. 2014). Although the Brick does not yet harbor fully formed massive stars or clusters, previous ALMA observations have shown evidence of ongoing intermediate- to high-mass star formation, including the detection of seven outflow features (D. L. Walker et al. 2021).

$CH_3CHO(5_{1,4} - 4_{1,3})$ and SO(2_3 − 1_2) were previously imaged towards the Brick cloud by J. M. Rathborne et al. (2015) with ALMA. Although the sensitivity and resolution are slightly higher in their data, we have imaged additional CS(2 − 1) and HC_3N(11 − 10) lines with a larger mosaic. In Fig. 9, the Brick cloud exhibits arm-like internal structures (K. G. Johnston et al.

Downloaded from academic.oup.com/mnras/article/552/2/stag253/8875762 by Liverpool John Moores University user on 02 November 2026

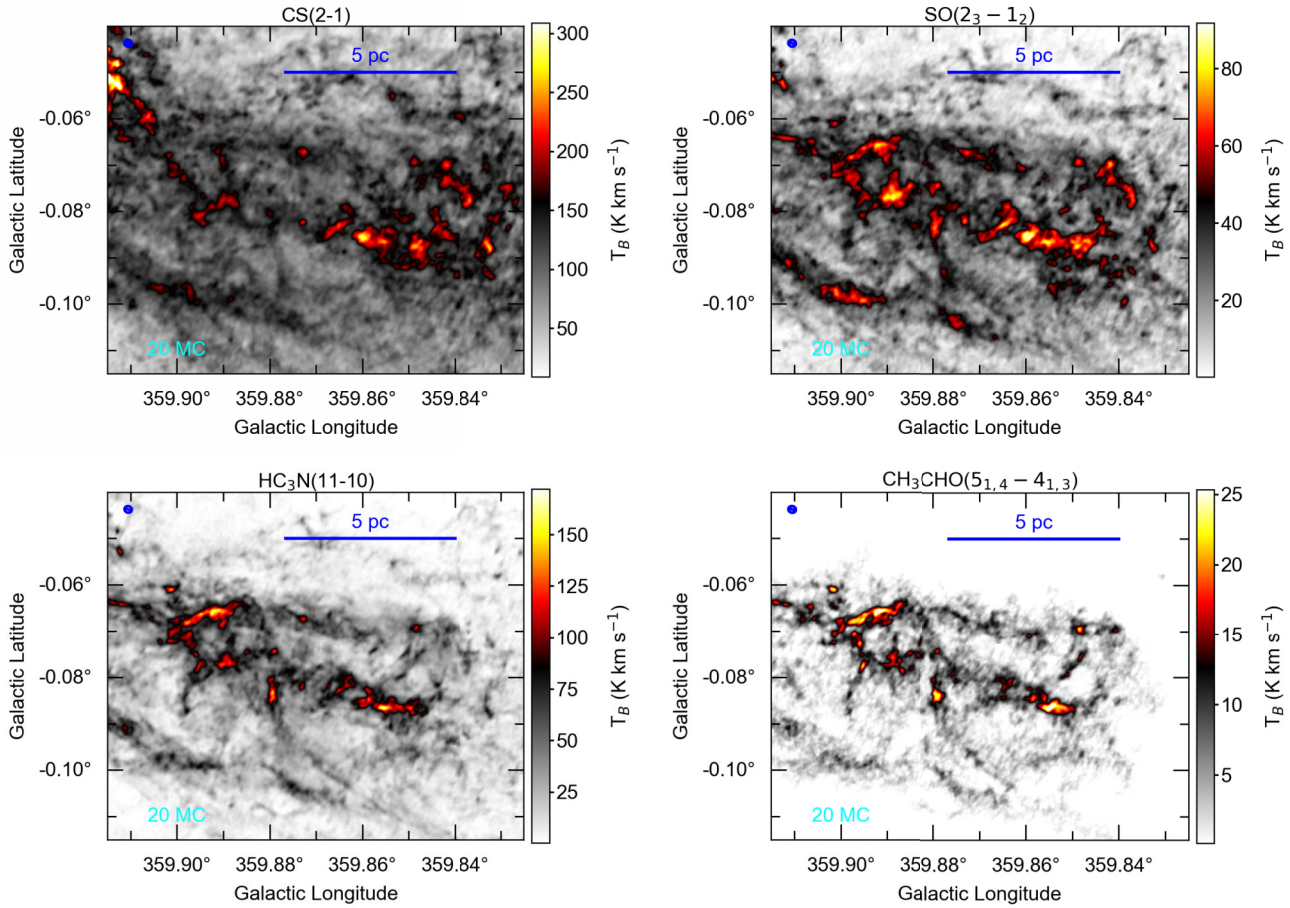


Figure 10. The `mom 0` images of the 20 km s^{-1} cloud. The CS(2 − 1), SO(2$_3$ − 1$_2$), HC$_3$N(11 − 10) and CH$_3$CHO(5$_{1,4}$ − 4$_{1,3}$) line images are presented. The synthesized beam is shown in the top left corner with an ellipse.

2014), and CH$_3$CHO(5$_{1,4}$ − 4$_{1,3}$) emission is relatively brighter in the southern part of the cloud. While both CS(2 − 1) and SO(2$_3$ − 1$_2$) exhibit widespread emission tracing the filaments and seem to be immersed in the diffuse arm-like structures in the CMZ, the emission from CH$_3$CHO(5$_{1,4}$ − 4$_{1,3}$) line is much more compact and spatially confined.

The CH$_3$CHO(5$_{1,4}$ − 4$_{1,3}$) emission appears to be well separated from the diffuse large-scale arms and instead traces distinct clumps concentrated within the central ridges of the Brick. The CH$_3$CHO(5$_{1,4}$ − 4$_{1,3}$) line exhibits morphologies similar to those of HC$_3$N(11 − 10), tracing a coherent network of compact clumps and ridges. These features are especially prominent along the southern ridge and central arc. This visual similarity is quantified by a high 2D morphological correlation coefficient of 0.9 (Fig. B1, more description in X. Lu, in preparation). The SO(2$_3$ − 1$_2$) line also shows significant overlap with HC$_3$N(11 − 10), capturing many of the same structures, though with slightly more diffuse emission. The SO(2$_3$ − 1$_2$)–HC$_3$N(11 − 10) correlation is also high, at 0.94, indicating strong morphological similarity. In contrast, the CS(2 − 1) emission displays a more extended and diffuse distribution, particularly towards the northern regions. It shows weaker overlap with both CH$_3$CHO(5$_{1,4}$ − 4$_{1,3}$) (correlation coefficient = 0.35) and HC$_3$N(11 − 10) (correlation coefficient = 0.66), but aligns relatively well with SO(2$_3$ − 1$_2$) (correlation coefficient = 0.8). The variation in internal structures among the four lines suggests that the compact features within the Brick vary chemically and physically.

3.3.3 *The 20 and 50 km s^{-1} cloud*

The 20 km s^{-1} cloud and the 50 km s^{-1} cloud are prominent giant molecular clouds in the CMZ (e.g. K. Uehara et al. 2019; X. Lu et al. 2021), specifically, near the Sgr A∗. The 20 km s^{-1} cloud shows signs of early-stage star formation, including the detection of protostellar outflows in the SiO(5–4) line (X. Lu et al. 2021). In contrast, the 50 km s^{-1} cloud does not exhibit clear protostellar outflow signatures and currently has low star formation rate ($\lesssim 0.3 \times 10^{-3}$ M$_\odot$, X. Lu et al. 2021), but it is likely in a later stage of star formation (E. Mills et al. 2011), as it lies adjacent to the compact H II region complex G−0.02 − 0.07 (Fig. A1 in this paper) (M. Tsuboi et al. 2019; E. Mills et al. 2011), which shares a similar velocity structure. While the 50 km s^{-1} cloud is currently inactive in star formation, R. Miyawaki et al. (2021) reported the detection of 28 hot molecular core candidates, which are in quasi-static equilibrium.

Figs 10 and 11 show the detection of CH$_3$CHO(5$_{1,4}$ − 4$_{1,3}$) emission towards the 20 and 50 km s^{-1} clouds, respectively. As in the Brick cloud, CH$_3$CHO shows a high correlation with HC$_3$N (0.9), a moderate correlation with SO (0.69), and a low correlation with CS (0.34).

Downloaded from academic.oup.com/mnras/article/552/2/stag253/8875762 by Liverpool John Moores University user on 02 November 2026

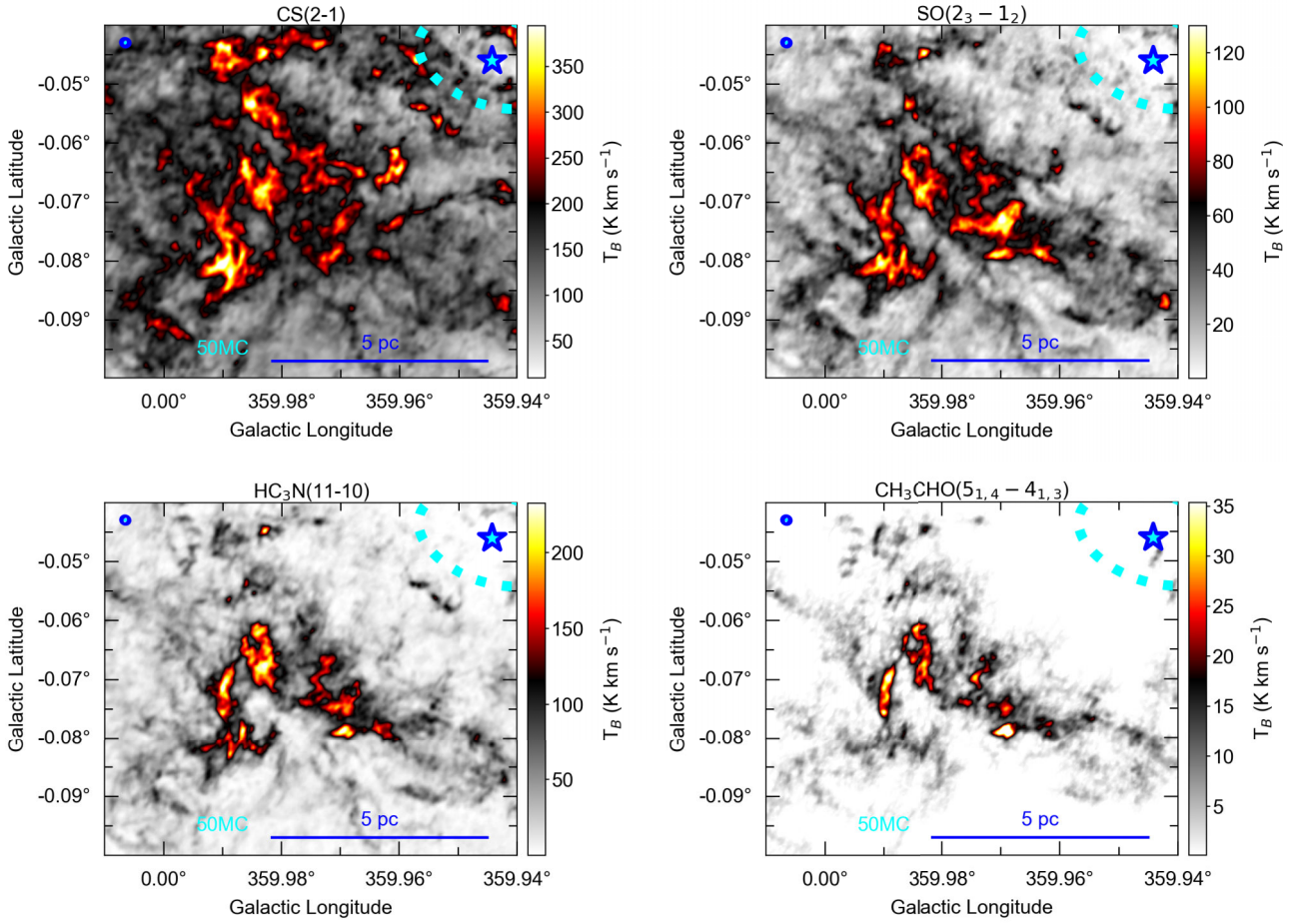


Figure 11. The `mom 0` images of the 50 km s^{-1} cloud. The Sgr A∗ is labelled with the star marker. The CND is outlined with a dotted arc. The CS($2-1$), SO(2_3-1_2), $HC_3N(11-10)$ and $CH_3CHO(5_{1,4}-4_{1,3})$ line images are presented. The synthesized beam is shown in the top left corner with an ellipse.

3.3.4 The three little pigs (TLP)

The Three Little Pigs (TLP) cloud complex consists of four molecular clouds known as the Straw (M0.145-0.086), the Sticks (M0.106-0.082), and the Stone (M0.068-0.075) (C. Battersby et al. 2020) from the left to the right side in Fig. 12. Consistent with the previous SMA 1 mm image (C. Battersby et al. 2020), the morphology of the TLP clouds appears to become progressively more complex from the straw cloud to the stone cloud. The straw cloud is very faint in lines, possibly quiescent or less evolved. The stick cloud appears to be the most prominent in these four molecular lines, showing compact clumps in all three tracers. Similar to the aforementioned clouds, we find a consistent trend in the morphological correlations among these four lines: CH_3CHO shows the highest correlation with HC_3N (0.89), an intermediate correlation with SO (0.77), and the lowest correlation with CS (0.59).

4 MORPHOLOGICAL CORRELATIONS BETWEEN THE CS($2-1$), SO(2_3-1_2), $HC_3N(11-10)$, $CH_3CHO(5_{1,4}-4_{1,3})$ AND SIO(2-1)

In Fig. B1, we find that $CH_3CHO(5_{1,4}-4_{1,3})$ shows the highest correlation with $HC_3N(11-10)$ (0.84-0.9 across the four highlighted regions), an intermediate correlation with SO(2_3-1_2) (0.64-0.69), and the weakest correlation with CS($2-1$) (0.25-0.59). This consistent pattern across all regions suggests that $CH_3CHO(5_{1,4}-4_{1,3})$ emission is more spatially similar to $HC_3N(11-10)$ than to CS($2-1$). Although the CS molecule is widely used dense-gas tracer because of the large dipole moment and high critical densities, its high abundance often leads to significant optical depth, limiting its reliability for tracing the most compact, high-column structures. J. Pety et al. (2017) showed that CS emission mainly traces gas at intermediate column densities and saturates in the densest regions, while CS(1-0) in the CMZ shows moderate optical depths of $\tau \lesssim$ 2-3 (M. Tsuboi, T. Handa & N. Ukita 1999), consistent with its widespread distribution across the CMZ clouds.

The critical densities of CS($2-1$) and SO(2_3-1_2) are roughly an order of magnitude lower than those of $CH_3CHO(5_{1,4}-4_{1,3})$ and $HC_3N(11-10)$. Although we have not directly derived the gas densities here, at first glance, the correlation coefficients suggest that CS($2-1$) and SO(2_3-1_2) trace more extended dense gas, whereas $CH_3CHO(5_{1,4}-4_{1,3})$ and $HC_3N(11-10)$ highlight more compact, denser substructures. However, $CH_3CHO(5_{1,4}-4_{1,3})$ emission does not necessarily trace dense cores exclusively (M. Ikeda et al. 2001; J. K. Jørgensen et al. 2016; C. Codella et al. 2017; Y. Oya et al. 2017); given its relatively low abundance and the subthermal excitation of its low-J transitions at moderate densities ($\sim 10^{4-5}$ cm^{-3}), its detection may be biased towards high-column-density regions that exceed the sensitivity threshold rather than reflecting a true absence elsewhere (e.g. M. A.

Downloaded from academic.oup.com/mnras/article/552/2/stag253/8875762 by Liverpool John Moores University user on 02 November 2026

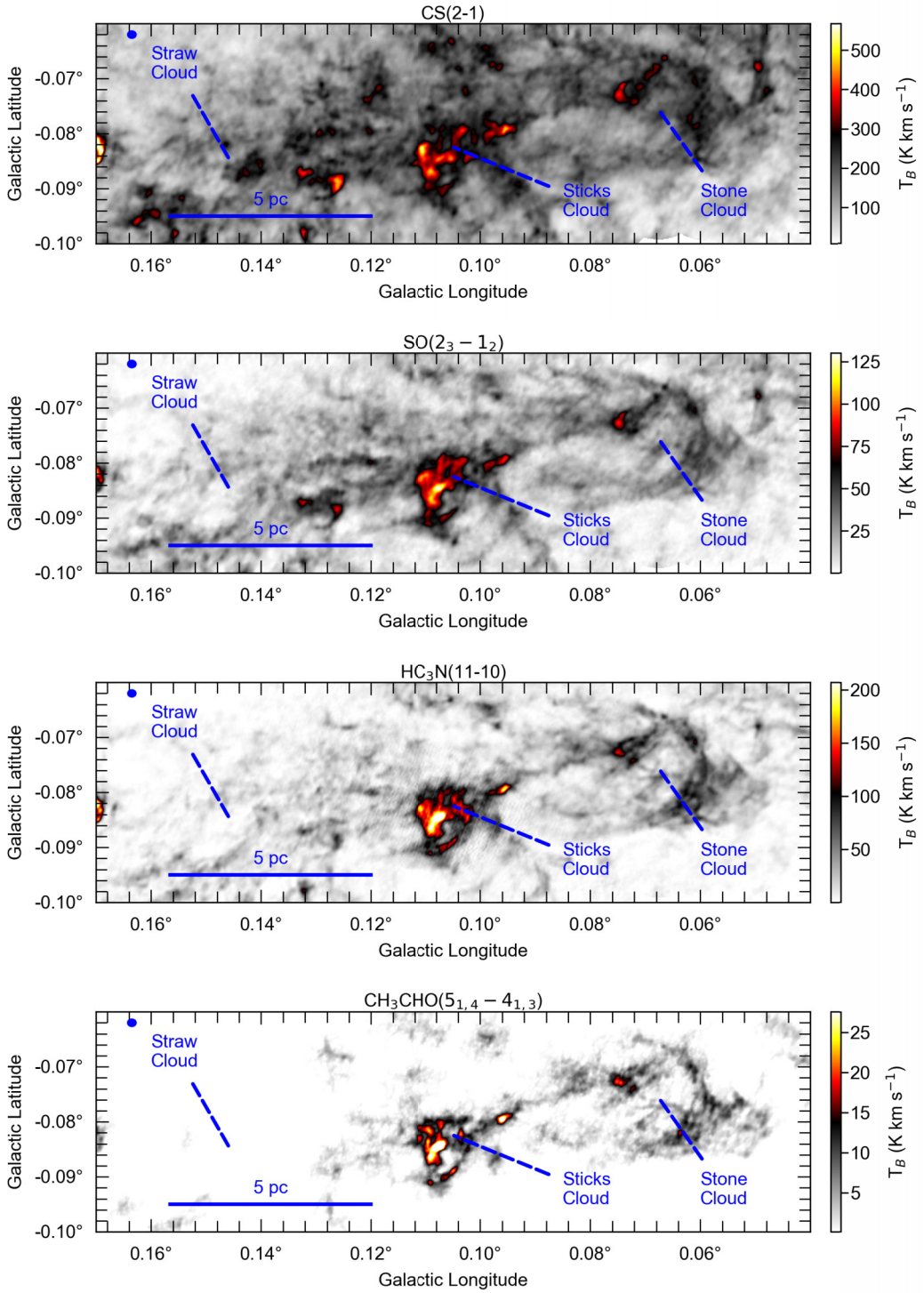


Figure 12. The `mom 0` images of the three little pigs cloud (stone, sticks, and straw cloud). The CS($2-1$), SO($2_3 - 1_2$), $HC_3N(11-10)$ and $CH_3CHO(5_{1,4} - 4_{1,3})$ line images are presented. The synthesized beam is shown in the top left corner with an ellipse.

Requena-Torres et al. 2006; I. Jimenez-Serra, C. Codella & A. Belloche 2025). Observations of optically thin isotopologues such as $HC^{15}N$ (Paper III) could therefore help disentangle optical-depth effects and confirm the effectiveness of these molecules as dense-gas tracers.

In Fig. B1, SO($2_3 - 1_2$), $HC_3N(11-10)$, and $CH_3CHO(5_{1,4} - 4_{1,3})$ show stronger correlations with SiO than with CS across the four regions and in the CMZ average (Paper III). SiO is a well-established shock tracer (P. Schilke et al. 1997), and its widespread CMZ emission likely reflects large-scale shocks driven by, for example, expanding H II regions or supernova remnants (S. Inutsuka 2021; J. D. Henshaw et al. 2022), cloud–cloud collisions (M. Tsuboi, A. Miyazaki & K. Uehara 2015; S. Zeng et al. 2020), or Galactic shear (J. M. D. Kruijssen et al. 2014; M. A.

Downloaded from academic.oup.com/mnras/article/552/2/stag253/8875762 by Liverpool John Moores University user on 02 November 2026

Petkova et al. 2021). Additional processes such as cosmic ray heating (F. Yusef-Zadeh et al. 2013) and X-ray irradiation (J. Martín-Pintado et al. 2000) may also influence Si-bearing chemistry.

Sulphur-bearing species such as SO can be enhanced in shock and post-shock gas (G. Pineau des Forets et al. 1993; D. C. Lis et al. 2001; X. Lu et al. 2017; D. Callanan et al. 2023), although SO is not unique to shocks and also appears in relatively quiescent gas in both low- and high-mass star-forming regions (e.g. A. Hacar et al. 2013). $HC_3N(11-10)$ is a well-known tracer of dense, early-phase cores, forming mainly through reactions involving CN and C_2H_2 radicals (e.g. C. M. Walmsley, G. Winnewisser & F. Toelle 1980; H. Suzuki et al. 1992), but its abundance can also increase in low-velocity shocks associated with stellar outflows (e.g. R. Bachiller & M. Pérez Gutiérrez 1997; E. Mendoza et al. 2018; A. Hoque et al. 2025). $CH_3CHO(5_{1,4}-4_{1,3})$ is typically linked to hot cores and outflows in the Galactic disc (M. Ikeda et al. 2001; J. K. Jørgensen et al. 2016; C. Codella et al. 2017; Y. Oya et al. 2017), yet in the CMZ, COMs including $CH_3CHO(5_{1,4}-4_{1,3})$ are widespread and associated with low-velocity shocks largely independent of local star formation activity (M. A. Requena-Torres et al. 2006; I. Jimenez-Serra 2025; Z.-Y. Li et al. 2025).

Across these species, the correlation strengths with SiO-SO-SiO (0.90) > HC_3N-SiO (0.83) > CS-SiO (0.79) > CH_3CHO-SiO (0.67) suggest different physical and chemical conditions. A detailed determination of SiO abundances and dedicated chemical modelling, along with further examination of the associations among $SO(2_3-1_2)$, $HC_3N(11-10)$, and $CH_3CHO(5_{1,4}-4_{1,3})$, will be essential to better understand the extreme environment of the CMZ. These analyses are beyond the scope of this paper and the in-depth studies are left for future studies.

5 SUMMARY

In this paper, we present an overview of the ACES broadband spectral-line data and the public release of the $CS(2-1)$, $SO(2_3-1_2)$, $CH_3CHO(5_{1,4}-4_{1,3})$, H40α, and $HC_3N(11-10)$ mosaic images. We provide the corresponding moment maps, *l*-*v* diagrams, and a morphological correlation analysis comparing 14 lines with the 3 mm continuum (Paper II, Paper III, X. Lu, in preparation). The emissions from these molecules are widely distributed across the CMZ. The $CS(2-1)$ and $SO(2_3-1_2)$ lines exhibit more extended spatial distributions, whereas $HC_3N(11-10)$ and $CH_3CHO(5_{1,4}-4_{1,3})$ are more concentrated towards the denser regions. Comparisons with other lines, such as SO transitions and isotopologues (Paper I) will also be useful for constraining the temperature and density.

The morphological correlation analysis reveals systematic differences in how molecular species trace the physical and chemical structures within the CMZ. The stronger correlations of $SO(2_3-1_2)$, $HC_3N(11-10)$, and $CH_3CHO(5_{1,4}-4_{1,3})$ with SiO indicate that these species are more closely linked to shocked gas. These results highlight the potential of the CMZ as a laboratory for studying the properties and history of large-scale shocks and their impact on molecular chemistry. Although we have not determined SiO or other shock-related abundances here, the observed correlations provide valuable constraints for future investigations at high spatial resolution. In addition to shocks, other energetic drivers such as cosmic rays, X-rays, and photodissociation regions, as indicated by the H II regions traced by H40α, are also likely to influence the chemical and thermal state of the gas. A comprehensive study of these processes, combining chemical modelling and multi-line diagnostics, will be essential to deepen our understanding of the interplay between dynamics and chemistry in the CMZ.

SOFTWARE

This paper made use of the following software packages: CASA (CASA Team et al. 2022) to carry out calibration and imaging of the ALMA data, CARTA (A. Comrie et al. 2021) to visualize and analyse the data, ASTROPY (Astropy Collaboration et al. 2013; A. M. Price-Whelan et al. 2018; Astropy Collaboration et al. 2022) to analyse the images and make plots, SPECTRAL-CUBE (A. Ginsburg et al. 2019) to process the image cubes and produce the moment maps, RADIO-BEAM (E. Koch et al. 2025) to determine (1) a common beam among multiple channels in a cube, (2) to smooth the individual channel beams to this common resolution, and (3) to determine the Jy-K conversion, and APLPY (T. Robitaille & E. Bressert 2012) and SEABORN (M. L. Waskom 2021) to make plots.

ACKNOWLEDGEMENTS

We thank the anonymous referee for the careful reading and constructive comments that helped improve this paper. This paper makes use of the following ALMA data: ADS/JAO.ALMA#2021.1.00172.L. ALMA is a partnership of ESO (representing its member states), NSF (USA) and NINS (Japan), together with NRC (Canada), NSTC and ASIAA (Taiwan), and KASI (Republic of Korea), in cooperation with the Republic of Chile. The Joint ALMA Observatory is operated by ESO, AUI/NRAO and NAOJ. The authors are grateful to the staff throughout the ALMA organization, particularly those at the European ALMA Regional Centre, the Joint ALMA Observatory, and the UK ALMA Regional Centre Node, for their extensive support, which was essential to the success of this challenging Large Program.

Data analysis was in part carried out on the Multi-wavelength Data Analysis System operated by the Astronomy Data Center (ADC), National Astronomical Observatory of Japan. DLW gratefully acknowledges support from the UK ALMA Regional Centre (ARC) Node, which is supported by the Science and Technology Facilities Council [grant numbers ST/Y004108/1 and ST/T001488/1]. CB gratefully acknowledges funding from National Science Foundation under Award Nos. 2108938, 2206510, and CAREER 2145689, as well as from the National Aeronautics and Space Administration through the Astrophysics Data Analysis Program under Award ``3-D MC: Mapping Circumnuclear Molecular Clouds from X-ray to Radio,'' Grant No. 80NSSC22K1125. RF acknowledges support from the grants PID2023-146295NB-I00, and from the Severo Ochoa grant CEX2021-001131-S funded by MCIN/AEI/10.13039/501100011033 and by 'European Union NextGenerationEU/PRTR'. IJ-S, LC, and VMR acknowledge support from the grant PID2022-136814NB-I00 by the Spanish Ministry of Science, Innovation and Universities/State Agency of Research MICIU/AEI/10.13039/501100011033 and by European Regional Development Fund (ERDF), UE. IJ-S also acknowledges the European Research Council (ERC) Consolidator grant OPENS (project number 101125858) funded by the European Union. VMR also acknowledges the grant RYC2020-029387-I funded by MICIU/AEI/10.13039/501100011033 and by 'ESF, Investing in your future', and from the Consejo Superior de Investigaciones Científicas (CSIC) and the Centro de Astrobiología (CAB) through the project 20225AT015 (Proyectos intramurales

Downloaded from academic.oup.com/mnras/article/552/2/stag253/8875762 by Liverpool John Moores University user on 02 November 2026

especiales del CSIC); and from the grant CNS2023-144464 funded by MICIU/AEI/10.13039/501100011033 and by 'European Union NextGenerationEU/PRTR. The authors acknowledge UFIT Research Computing for providing computational resources and support that have contributed to the research results reported in this publication. AG acknowledges support from the National Science Foundation (NSF) under grants CAREER 2142300, AAG 2008101, and particularly AAG 2206511 that supports the ACES large program. MGS-M acknowledges support from the National Science Foundation (NSF) under grant CAREER 2142300. MGS-M also thanks the Spanish Ministry of Science, Innovation and Universities (MICINN) for funding support under grants PID2022-137980NB-I00 and PID2023-146667NB-I00. AS-M acknowledges support from the RyC2021-032892-I grant funded by MCIN/AEI/10.13039/501100011033 and by the European Union 'Next GenerationEU'/PRTR, as well as the program Unidad de Excelencia María de Maeztu CEX2020-001058-M, and support from the PID2023-146675NB-I00 (MCI-AEI-FEDER, UE). KMD acknowledges support from the European Research Council (ERC) Advanced Grant MOPPEX 833460.vii. XL acknowledges support from the Strategic Priority Research Program of the Chinese Academy of Sciences (CAS) Grant No. XDB0800300, the National Key R&D Program of China (No. 2022YFA1603101), State Key Laboratory of Radio Astronomy and Technology (CAS), the National Natural Science Foundation of China (NSFC) through grant Nos. 12273090 and 12322305, the Natural Science Foundation of Shanghai (No. 23ZR1482100), and the CAS 'Light of West China' Program No. xbzg-zdsys-202212. Q Z gratefully acknowledges the support from the National Science Foundation under Award No. AST-2206512, and the Smithsonian Institute FY2024 Scholarly Studies Program. FHL acknowledges support from the ESO Studentship Programme, the Scatcherd European Scholarship of the University of Oxford, and the European Research Council's starting grant ERC StG-101077573 ('ISM-METALS'). C F acknowledges funding provided by the Australian Research Council (Discovery Projects DP230102280 and DP250101526), and the Australia-Germany Joint Research Cooperation Scheme (UA-DAAD). FM acknowledges financial support from the School of Astronomy at the Institute for Research in Fundamental Sciences-IPM. JK is supported by the Royal Society under grant number RF\ERE\231132, as part of project URF\R1\211322. MCS acknowledges financial support from the European Research Council under the ERC Starting Grant 'GalFlow' (grant 101116226) and from Fondazione Cariplo under the grant ERC attrattività n. 2023-3014. MC gratefully acknowledges funding from the DFG through an Emmy Noether Research Group (grant number CH2137/1-1). COOL Research DAO (M. Chevance, J. M. D. Kruijssen & S. N. Longmore 2025) is a Decentralized Autonomous Organization supporting research in astrophysics aimed at uncovering our cosmic origins. JW gratefully acknowledges funding from National Science Foundation under Award Nos. 2108938 and 2206510. EACM gratefully acknowledges funding from the National Science Foundation under Award Nos. 1813765, 2115428, 2206509, and CAREER 2339670. FN-L gratefully acknowledges financial support from grant PID2024-162148NA-I00, funded by MCIN/AEI/10.13039/501100011033 and the European Regional Development Fund (ERDF) 'A way of making Europe', from the Ramón y Cajal programme (RYC2023-044924-I) funded by MCIN/AEI/10.13039/501100011033 and FSE + , and from the Severo Ochoa grant CEX2021-001131-S, funded by MCIN/AEI/10.13039/501100011033. RSK acknowledges financial support for the ERC Synergy Grant ``ECOGAL" (855130) and for the Heidelberg Excellence Cluster ``STRUCTURES" (EXC 2181 - 390900948). In addition RSK is grateful for funding for project ``MAINN" (BMWK, 50OO2206) and for project ``STARCLUSTERS" (DFG KL 1358/22-1). S.Z. acknowledges support from the NAOJ ALMA Scientific Research Grant Code 2025-29B.

DATA AVAILABILITY

All data products and associated documentation can be found at https://almascience.org/alma-data/lp/aces. To maximize usability and provide a single, comprehensive resource for users, we also provide an online, machine-readable table, which contains the full, detailed list of all data products released for the entire survey, including hyperlinks to the full files from the ALMA archive.

All code and data processing issues are available at the public GitHub repository here: https://github.com/ACES-CMZ/reduction_ACES.

The ACES data reduction was a monolithic work that was written up in five papers. If you use the ACES data, please cite the appropriate works, which include S. Longmore & ACES Team (2025) and the data papers: continuum (A. Ginsburg & ACES Team 2025) and cubes in high-resolution (this work), medium-resolution (X. Lu, in preparation), and low-resolution (P. Hsieh 2025) spectral windows. Note that all papers should be cited for use of any data; the continuum imaging relied on the line papers, and vice versa.

REFERENCES

Ao Y. et al., 2013, A&A, 550s, A135
Astropy Collaboration et al., 2013, A&A, 558, A33
Astropy Collaboration et al., 2022, ApJ, 935, 167
Bachiller R., Pérez Gutiérrez M., 1997, ApJ, 487, L93
Barnes A. T., Longmore S. N., Battersby C., Bally J., Kruijssen J. M. D., Henshaw J. D., Walker D. L., 2017, MNRAS, 469, 2263
Battersby C. et al., 2020, ApJS, 249, 35
CASA Team et al., 2022, PASP, 134, 114501
Callanan D. et al., 2023, MNRAS, 520, 4760
Chevance M., Kruijssen J. M. D., Longmore S. N., 2025, preprint (arXiv:2501.13160)
Codella C. et al., 2017, A&A, 605, L3
Comrie A. et al., 2021, CARTA: Cube Analysis and Rendering Tool for Astronomy, Astrophysics Source Code Library, record ascl:2103.031 (ascl:2103.031)
De Pree C. G., Wilner D. J., Goss W. M., 2011, AJ, 142, 177
Ekers R. D., van Gorkom J. H., Schwarz U. J., Goss W. M., 1983, A&A, 122, 143
Figer D. F., Kim S. S., Morris M., Serabyn E., Rich R. M., McLean I. S., 1999, ApJ, 525, 750
Genzel R., Eisenhauer F., Gillessen S., 2010, Rev. Mod. Phys., 82, 3121
Ginsburg A., ACES Team, 2025, ApJ, 1, 1 (Paper II)
Ginsburg A. et al., 2016, A&A, 586, A50
Ginsburg A. et al., 2019, radio-astro-tools/spectral-cube: Release v0.4.5, Zenodo
Hacar A., Tafalla M., Kauffmann J., Kovács A., 2013, A&A, 554, A55
Harada N. et al., 2015, A&A, 584, A102
Henshaw J. D. et al., 2016, MNRAS, 457, 2675
Henshaw J. D. et al., 2022, MNRAS, 509, 4758
Henshaw J. D., Barnes A. T., Battersby C., Ginsburg A., Sormani M. C., Walker D. L., 2023, in Inutsuka S., Aikawa Y., Muto T., Tomida K., Tamura M., eds, ASP Conf. Ser. Vol. 534, Protostars and Planets VII. Astron. Soc. Pac., San Francisco, p. 83

Downloaded from academic.oup.com/mnras/article/552/2/stag253/8875762 by Liverpool John Moores University user on 02 November 2026

Ho P. T. P., Jackson J. M., Barrett A. H., Armstrong J. T., 1985, ApJ, 288, 575
Hoque A. et al., 2025, ApJ, 987, 197
Hsieh P., 2025, preprint
Hsieh P.-Y., Ho P. T. P., Hwang C.-Y., Shimajiri Y., Matsushita S., Koch P. M., Iono D., 2016, ApJ, 831, 72
Hsieh P.-Y., Koch P. M., Ho P. T. P., Kim W.-T., Tang Y.-W., Wang H.-H., Yen H.-W., Hwang C.-Y., 2017, ApJ, 847, 3
Hsieh P.-Y. et al., 2021, ApJ, 913, 94
Ikeda M., Ohishi M., Nummelin A., Dickens J. E., Bergman P., Hjalmarson Å., Irvine W. M., 2001, ApJ, 560, 792
Immer K., Menten K. M., Schuller F., Lis D. C., 2012, A&A, 548, A120
Immer K., Kauffmann J., Pillai T., Ginsburg A., Menten K. M., 2016, A&A, 595, A94
Inutsuka S., 2021, in Tsuboi M., Oka T., eds, ASP Conf. Ser. Vol. 528, New Horizons in Galactic Center Astronomy and Beyond. Astron. Soc. Pac., San Francisco, p. 271
Jimenez-Serra I., 2025, preprint (arXiv:2501.01782)
Jimenez-Serra I., Codella C., Belloche A., 2025, preprint (arXiv:2503.17104)
Johnston K. G., Beuther H., Linz H., Schmiedeke A., Ragan S. E., Henning T., 2014, A&A, 568, A56
Jones P. A., Burton M. G., Tothill N. F. H., Cunningham M. R., 2011, MNRAS, 411, 2293
Jones P. A. et al., 2012, MNRAS, 419, 2961
Jørgensen J. K. et al., 2016, A&A, 595, A117
Kauffmann J., Pillai T., Zhang Q., 2013, ApJ, 765, L35
Koch E. et al., 2025, radio-astro-tools/radio-beam: v0.3.9. Zenodo
Krieger N. et al., 2017, ApJ, 850, 77
Kruijssen J. M. D., Longmore S. N., 2013, MNRAS, 435, 2598
Kruijssen J. M. D., Longmore S. N., Elmegreen B. G., Murray N., Bally J., Testi L., Kennicutt R. C., 2014, MNRAS, 440, 3370
Kruijssen J. M. D. et al., 2019, MNRAS, 484, 5734
Krumholz M. R., Kruijssen J. M. D., 2015, MNRAS, 453, 739
Krumholz M. R., Kruijssen J. M. D., Crocker R. M., 2017, MNRAS, 466, 1213
Lang C. C., Goss W. M., Wood O. S., 1997, ApJ, 474, 275
Lang C. C., Goss W. M., Morris M., 2002, AJ, 124, 2677
Li Z.-Y. et al., 2025, A&A, 697, A190
Lindberg J. E., Aalto S., Costagliola F., Pérez-Beaupuits J.-P., Monje R., Muller S., 2011, A&A, 527, A150
Lipman D. et al., 2025, ApJ, 984, 159
Lis D. C., Carlstrom J. E., 1994, ApJ, 424, 189
Lis D. C., Serabyn E., Zylka R., Li Y., 2001, ApJ, 550, 761
Liu H. B., Ho P. T. P., Wright M. C. H., Su Y.-N., Hsieh P.-Y., Sun A.-L., Kim S. S., Minh Y. C., 2013, ApJ, 770, 44
Longmore S., ACES Team, 2025, ApJ, 1, 1 (Paper I)
Longmore S. N. et al., 2013, MNRAS, 429, 987
Lu X. et al., 2017, ApJ, 839, 1
Lu X. et al., 2019a, ApJS, 244, 35
Lu X. et al., 2019b, ApJ, 872, 171
Lu X. et al., 2021, ApJ, 909, 177
Martín-Pintado J., de Vicente P., Rodríguez-Fernández N. J., Fuente A., Planesas P., 2000, A&A, 356, L5
Martín S., Martín-Pintado J., Montero-Castaño M., Ho P. T. P., Blundell R., 2012, A&A, 539, A29
Mehringer D. M., Yusef-Zadeh F., Palmer P., Goss W. M., 1992, ApJ, 401, 168
Mehringer D. M., Palmer P., Goss W. M., Yusef-Zadeh F., 1993, ApJ, 412, 684
Meier D. S., Turner J. L., 2005, ApJ, 618, 259
Mendoza E. et al., 2018, MNRAS, 475, 5501
Mills E., Morris M. R., Lang C. C., Dong H., Wang Q. D., Cotera A., Stolovy S. R., 2011, ApJ, 735, 84
Mills E. A. C., Güsten R., Requena-Torres M. A., Morris M. R., 2013, ApJ, 779, 47
Miyawaki R., Tsuboi M., Uehara K., Miyazaki A., 2021, PASJ, 73, 943
Morris M., Serabyn E., 1996, ARA&A, 34, 645
Oya Y. et al., 2017, ApJ, 837, 174
Petkova M. A. et al., 2023 MNRAS 520 2245
Pety J. et al., 2017, A&A, 599, A98
Pickett H. M., Poynter R. L., Cohen E. A., Delitsky M. L., Pearson J. C., Müller H. S. P., 1998, J. Quant. Spec. Radiat. Transf., 60, 883
Pineau des Forets G., Roueff E., Schilke P., Flower D. R., 1993, MNRAS, 262, 915
Price-Whelan A. M. et al., 2018, AJ, 156, 123
Rathborne J. M. et al., 2014, ApJ, 795, L25
Rathborne J. M. et al., 2015, ApJ, 802, 125
Requena-Torres M. A., Martín-Pintado J., Rodríguez-Franco A., Martín S., Rodríguez-Fernández N. J., de Vicente P., 2006, A&A, 455, 971
Requena-Torres M. A. et al., 2012, A&A, 542, L21
Robitaille T., Bressert E., APLpy: Astronomical Plotting Library in Python Astrophysics Source Code Library, record ascl:1208.017
Rodriguez-Franco A., Martin-Pintado J., Fuente A., 1998, A&A, 329, 1097
Sault R. J., Teuben P. J., Wright M. C. H., 1995, in Shaw R. A., Payne H. E., Hayes J. J. E., eds, ASP Conf. Ser. Vol. 77, Astronomical Data Analysis Software and Systems IV. Astron. Soc. Pac., San Francisco, p. 433
Schilke P., Walmsley C. M., Pineau des Forets G., Flower D. R., 1997, A&A, 321, 293
Schöier F. L., van der Tak F. F. S., van Dishoeck E. F., Black J. H., 2005, A&A, 432, 369
Simpson J. P., Colgan S. W. J., Cotera A. S., Kaufman M. J., Stolovy S. R., 2018, ApJ, 867, L13
Simpson J. P., Colgan S. W. J., Cotera A. S., Kaufman M. J., Stolovy S. R., 2021, ApJ, 910, 59
Sofue Y. et al., 2025 PASJ 77 L55
Sormani M. C. et al., 2022, MNRAS, 512, 1857
Steinke M., Oskinova L. M., Hamann W. R., Sander A., Liermann A., Todt H., 2016, A&A, 588, A9
Suzuki H., Yamamoto S., Ohishi M., Kaifu N., Ishikawa S.-I., Hirahara Y., Takano S., 1992, ApJ, 392, 551
Tacconi L. J. et al., 2008, ApJ, 680, 246
Tress R. G., Sormani M. C., Glover S. C. O., Klessen R. S., Battersby C. D., Clark P. C., Hatchfield H. P., Smith R. J., 2020, MNRAS, 499, 4455
Tsuboi M., Handa T., Ukita N., 1999, ApJS, 120, 1
Tsuboi M., Miyazaki A., Uehara K., 2015, PASJ, 67, 109
Tsuboi M., Kitamura Y., Uehara K., Miyazaki A., Miyawaki R., Tsutsumi T., Miyoshi M., 2019, PASJ, 71, 128
Uehara K., Tsuboi M., Kitamura Y., Miyawaki R., Miyazaki A., 2019, ApJ, 872, 121
Walker D., ACES Team, 2025, ApJ, 1, 1 (Paper III)
Walker D. L. et al., 2021, MNRAS, 503, 77
Walker D. L. et al., 2025, ApJ, 984, 158
Walmsley C. M., Winnewisser G., Toelle F., 1980, A&A, 81, 245
Waskom M. L., 2021, J. Open Source Softw., 6, 3021
Yusef-Zadeh F., Wardle M., Lis D., Viti S., Brogan C., Chambers E., Pound M., Rickert M., 2013, J. Phys. Chem. A, 117, 9404
Zeng S. et al., 2020, MNRAS, 497, 4896
Zhao J.-H., Morris M. R., Goss W. M., An T., 2009, ApJ, 699, 186

APPENDIX A: ZOOM-INS OF H40α LINE

The H40α map indicative of ionized gas associated with the H II regions in the Sgr A mini-spiral (e.g. J.-H. Zhao et al. 2009) and H II region G-0.02-0.07 (e.g. R. D. Ekers et al. 1983; E. Mills et al. 2011; K. Uehara et al. 2019), the possible H II region detected in the 20 km s^{-1} cloud (P. T. P. Ho et al. 1985; X. Lu et al. 2019b), the Sgr B1 (e.g. D. M. Mehringer et al. 1992; J. P. Simpson et al. 2018, 2021) and Sgr B2 (e.g. D. M. Mehringer et al. 1993; C. G. De Pree, D. J. Wilner & W. M. Goss 2011; P. A. Jones et al. 2011), the Arched filaments (e.g. C. C. Lang, W. M. Goss & M. Morris 2002), the pistol and sickle (e.g. C. C. Lang, W. M. Goss & O. S. Wood 1997; M. Steinke et al. 2016). These sources are significantly detected in the ACES data.

Downloaded from academic.oup.com/mnras/article/552/2/stag253/8875762 by Liverpool John Moores University user on 02 November 2026

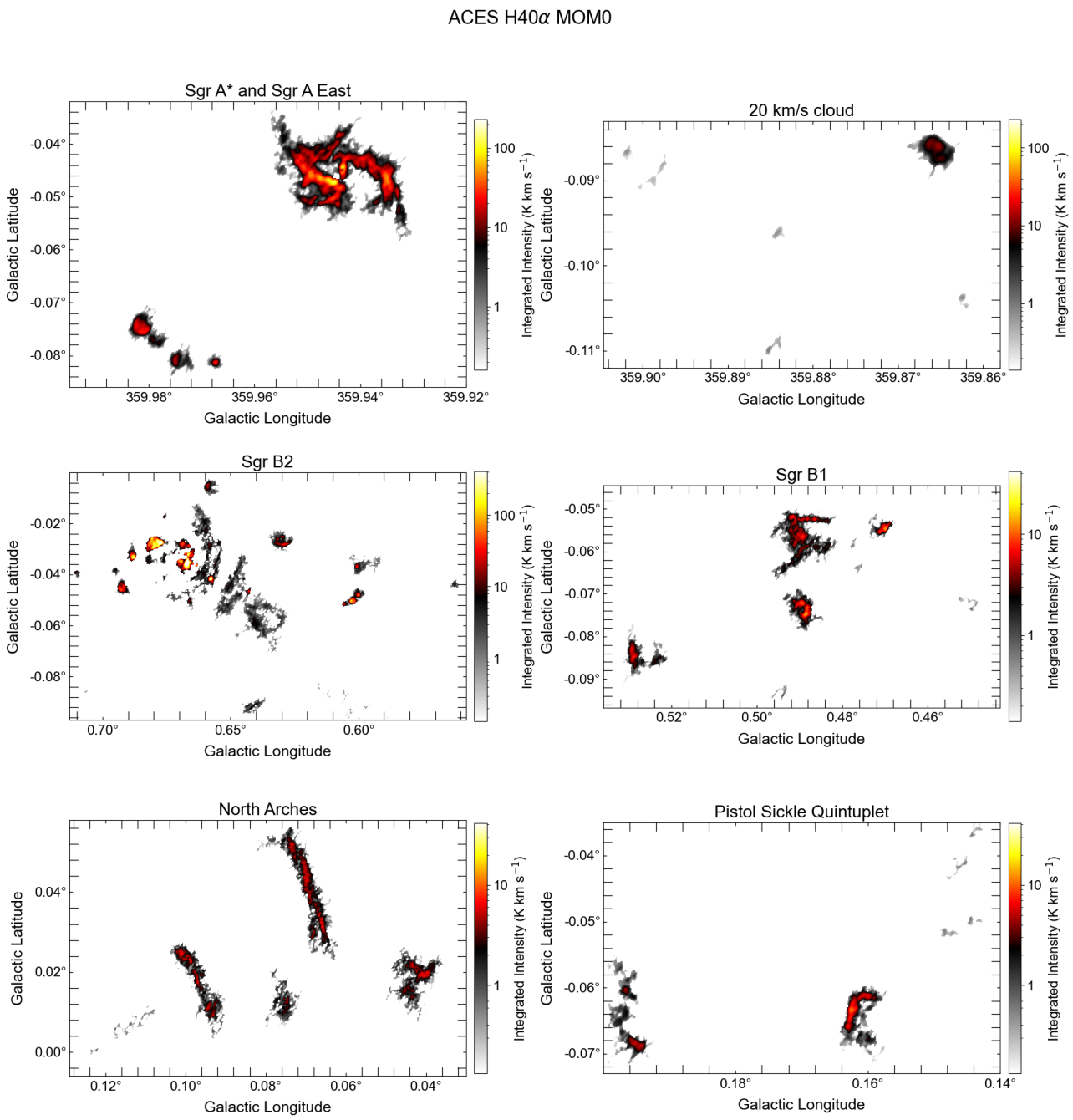


Figure A1. 2The zoom-in views of the ACES H40αmom0 images show regions with significant detections. For easy comparison, the names of the regions follow the nomenclature adopted in A. Ginsburg & ACES Team (2025).

APPENDIX B: 2D CORRELATION MATRIX

In Fig. B1, we present the two-dimensional (2D) Pearson correlation coefficients among the 14 lines and the continuum images. A detailed description of the method is provided in X. Lu (in preparation). The regions used for these calculations are listed in Table B1.

We include the correlation matrices to quantify how the spatial distributions of line intensities vary among different molecular tracers across each CMZ field. Each matrix element represents the normalized covariance between the brightness distributions of two spectral lines, measured over all valid pixels. A high correlation (1) means the lines vary together spatially, tracing similar gas structures or excitation conditions. A low correlation (0) indicates independent spatial variations, while a negative correlation (-1) implies anti-correlated emission. In general, molecular lines correlate strongly with one another, consistent with their tracing of dense gas structures. However, the overall correlation strength differs across regions: correlations are highest in the TLP, indicating that most molecular tracers vary together spatially,

Downloaded from academic.oup.com/mnras/article/552/2/stag253/8875762 by Liverpool John Moores University user on 02 November 2026

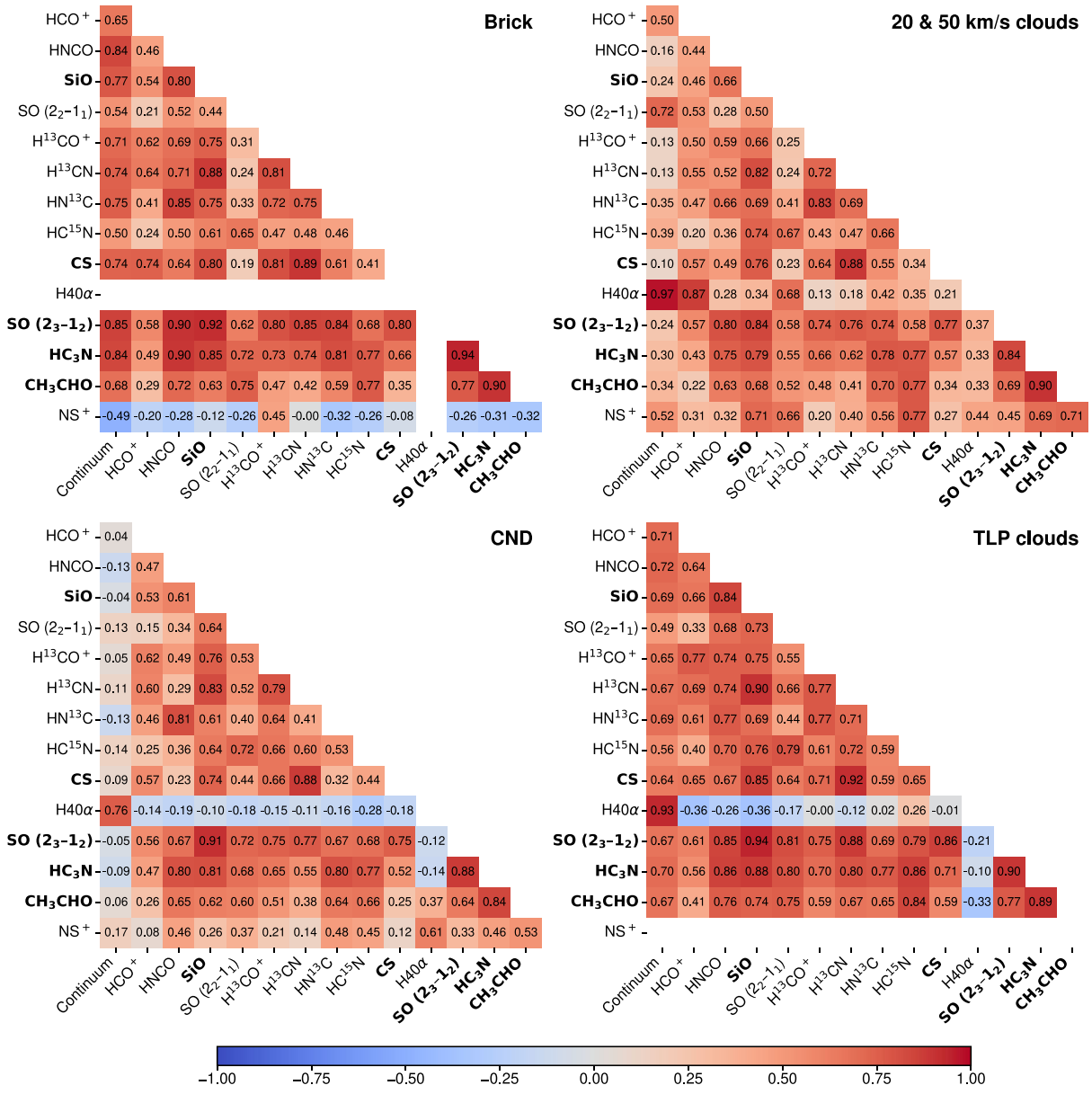


Figure B1. 2D correlation matrix between the continuum and integrated intensities (`mom 0` images) of the spectral lines presented in this paper, Paper III, and X. Lu (in preparation). In the fig. 12 of X. Lu (in preparation), all the pixels in the ACES mosaic fields are considered. In this paper we present the sub-fields towards the Brick cloud, the 20 and 50 km s^{-1} clouds, and CND, the TLP clouds, the Sgr C and Sgr B regions. Note that the Sgr A∗ is excluded in the CND region. The Sgr A∗ mask is centred on $(l, b) = (359.944^{\circ}, -0.046^{\circ})$, with a radius of 4.2″. Negative values mean anti-correlation, and the blank cells mean the invalid values in the images preventing calculation.

Table B1. DS9 regions in Galactic coordinates. Centres are in degrees; lengths are in arcseconds. For `box`, width/height are full sizes; for `ellipse`, the values are radii. Position angle (PA) in degrees.

Region	Shape	ℓ (deg)	b (deg)	Width/Radius$_x$ (arcsec)	Height/Radius$_y$ (arcsec)	PA (deg)
TLP clouds	Box	0.096408	−0.077577	364	129	0
CND	Ellipse	359.944183	−0.045176	121	164	68
Brick	Box	0.245984	0.011100	175	123	0
20 and 50 km s^{-1} cloud	Box	359.908	0.-0.0836	675	136	335

Downloaded from academic.oup.com/mnras/article/552/2/stag253/8875762 by Liverpool John Moores University user on 02 November 2026

whereas the CND exhibits the lowest correlations. The weaker correlations in the CND suggest that the emission arises from multiple, physically distinct components along the line of sight, leading to less coherent spatial correspondence between tracers. This highlights the increased structural and chemical complexity near Sgr A∗ compared to regions farther out in the CMZ. We note that the similarity analysis presented in this paper provides a first-order comparison. A more detailed analysis, selecting specific regions or structures, is essential to derive more accurate values.

APPENDIX C: DATA RELEASE SUMMARY

The data products from the ACES survey follow a uniform naming convention. The filenames for the data products presented in this paper can be constructed using the templates described below, in conjunction with the information provided in appendix A of D. Walker & ACES Team (2025).

The following subsections are divided according to different product types which occur at the Member ObsUnitSet (MOUS) and Group ObsUnitSet (GOUS) levels.[2]

C1 Member-level products (12 m and 7 m)

We release the data cubes for all SPWs for the 45 ACES regions. These are member-level products, and correspond to the cubes for the 12 m and 7 m arrays for each field prior to combination.

We release the cubes for the separate arrays as they are different to those initially delivered by ALMA due to the changes that were made during reprocessing. We do not re-release any of the standalone TP products, as we used the same cubes as those available in the ALMA Science Archive (ASA).

In this and subsequent subsections, we describe how to construct the filenames of the released data products by providing filename templates that include placeholder variables. These placeholders can be changed as needed to build the filename of the relevant product.

Following the requirements of the ASA, the filename template is:

`member.uid___A001_{`**mous-id**`}.lp_slongmore.{`**field_coords**`}.{`**array**`}.{`**frqrange**`}.cube.pbcor.fits`

The placeholder template components should be replaced as follows:

(i) {**mous-id**}: The 12 m or 7 m MOUS ID for a given field, as listed in Table A1 in D. Walker & ACES Team (2025).
(ii) {**field_coords**}: The central coordinates of the field, as listed in Table A1 in D. Walker & ACES Team (2025) (e.g. `G000.073 + 0.184`).
(iii) {**array**}: The ALMA array, either `12 m` or `7 m`.
(iv) {**frqrange**}: The frequency range, which depends on the SPW:

(a) SPW 33: `97.7-99.5GHz`
(b) SPW 35: `99.6-101.4GHz`

For example, to find the 12 m-only cube for CS for field `ao` (this field contains the well-known molecular cloud G0.253 + 0.016, aka the Brick), the resulting filename would be:

`member.uid___A001_X15a0_X190.lp_slongmore.G000.300 + 0.063.12m.97.7-99.5GHz.cube.pbcor.fits`

C2 Group-level products (Combined cubes per region)

We also release array-combined products per SPW per region. As these products combine data from multiple MOUSs, they are deemed to be group-level products. The filenames of these products can be constructed as follows:

`group.uid___A001_X1590_X30a9.lp_slongmore.{`**field_coords**`}.{`**arrays**`}.{`**frqrange**`}.cube.pbcor.fits`

Where the template components are:

(i) {**field_coords**} and {**frqrange**}: follow the same definition as for the member-level products.
(ii) {**arrays**}: `12m7mTP`

As an example, the corresponding CS cube including 12 m, 7 m, and TP data for field `ao` would be:

`group.uid___A001_X1590_X30a9.lp_slongmore.G000.300 + 0.063.12m7mTP.97.7-99.5GHz.cube.pbcor.fits`

C3 Group-level products (Full CMZ mosaics)

Finally, we release the full, contiguous mosaics covering the entire ACES footprint. Again, since these result from the combination of many MOUSs, the full mosaics are at the group level.

In contrast to cubes for the individual fields, we do not release full mosaics for all SPWs, but rather for specific lines. The lines relevant to this paper are given in Table 1. Most of the SPWs are sufficiently broad that they contain significant spectral ranges with no line emission. We therefore opted not to produce full mosaics containing these blank channels in the interest of reducing the file sizes. In addition to the data cubes for each line, we also release a suite of advanced products, including moment maps, noise maps, etc. (see below).

The filename template for the full mosaic cubes and associated products is:

`group.uid___A001_X1590_X30a9.lp_slongmore.cmz_mosaic.{`**arrays**`}.{`**molecule**`}.{`**suffix**`}`

Where the template components are:

(i) {**arrays**}: `12m7mTP`
(ii) {**molecule**}: `HC3N, CS21, H40a, CH3CHO, SO32`
(iii) {**suffix**} defines the specific data product. Products released with this paper are:

(a) `cube.pbcor.fits`: primary beam corrected image cube.
(b) `cube.downsampled_spatially.pbcor.fits`: as previous, spatially smoothed to a 5 arcsec beam and then spatially rebinned by a factor of 9 × 9.
(c) `integrated_intensity.fits`: masked integrated intensity map of the full-resolution cube.
(d) `mad_std.fits`: noise map of the full-resolution cube.
(e) `peak_intensity.fits`: peak intensity map of the full-resolution cube.
(f) `velocity_at_peak_intensity.fits`: velocity map from the masked full-resolution cube; velocity

[2]For a description of ALMA project structures and naming conventions, please refer to section 2 of the Cycle 9 QA2 guide: https://almascience.eso.org/documents-and-tools/cycle9/alma-qa2-data-products-for-cycle-9

Downloaded from academic.oup.com/mnras/article/552/2/stag253/8875762 by Liverpool John Moores University user on 02 November 2026

Table C1. Global statistics for SPW 33 and SPW 35 cubes for all ACES regions, with velocity offset V_{off} added as the second column.

Field	V_{off} (km s^{-1})	SPW_{12m}	B_{maj} (″)	B_{min} (″)	BPA (deg)	Image size (pix)	No. channels	Pixel size (″)	S_{peak} (mJy beam^{-1})	σ_{MAD} (mJy beam^{-1})
a	40	33	1.49	1.10	−67.0	(2070, 2482)	3840.0	0.20	128.3	3.9
a	40	35	1.42	1.06	−66.0	(2070, 2482)	3840.0	0.20	112.5	3.6
aa	0	33	1.63	1.44	−52.0	(1593, 1456)	3839.0	0.26	372.5	3.7
aa	0	35	1.63	1.41	−52.0	(1593, 1456)	3839.0	0.26	298.2	3.4
ab	0	33	1.63	1.52	−75.0	(1465, 1236)	3836.0	0.28	199.7	3.6
ab	0	35	1.60	1.48	−75.0	(1465, 1236)	3836.0	0.28	179.7	3.3
ac	0	33	1.54	1.06	−71.0	(1638, 1601)	3840.0	0.19	166.4	4.3
ac	0	35	1.51	1.03	−71.0	(1638, 1601)	3840.0	0.19	145.7	4.0
ad	0	33	1.79	1.78	−75.0	(1140, 2527)	3840.0	0.20	221.4	4.3
ad	0	35	1.77	1.75	−75.0	(1140, 2527)	3840.0	0.20	203.2	4.0
ae	0	33	1.88	1.52	83.0	(1313, 1344)	3840.0	0.30	253.0	3.8
ae	0	35	1.87	1.51	83.0	(1313, 1344)	3840.0	0.30	238.1	3.5
af	0	33	2.50	1.74	86.0	(1417, 1165)	3840.0	0.31	509.2	3.9
af	0	35	2.44	1.71	86.0	(1417, 1165)	3840.0	0.31	487.0	3.7
ag	0	33	1.65	1.26	−70.0	(1698, 1696)	3840.0	0.24	149.7	4.2
ag	0	35	1.62	1.24	−70.0	(1698, 1696)	3840.0	0.24	141.2	4.0
ah	30	33	1.66	1.12	−61.0	(1957, 1936)	3840.0	0.20	200.0	3.5
ah	30	35	1.64	1.09	−61.0	(1957, 1936)	3840.0	0.20	188.7	3.3
ai	0	33	2.11	1.52	79.0	(1350, 1601)	3840.0	0.29	285.0	3.7
ai	0	35	2.06	1.49	79.0	(1350, 1601)	3840.0	0.29	260.8	3.4
aj	−30	33	1.85	1.47	86.0	(1414, 1265)	3836.0	0.31	492.7	3.8
aj	−30	35	1.83	1.45	86.0	(1414, 1265)	3836.0	0.31	462.5	3.6
ak	30	33	1.96	1.67	80.0	(736, 988)	3836.0	0.32	256.3	3.8
ak	30	35	1.92	1.64	80.0	(736, 988)	3836.0	0.32	243.7	3.6
al	0	33	2.37	1.79	86.0	(2167, 1422)	3840.0	0.28	217.8	4.4
al	0	35	2.30	1.76	86.0	(2167, 1422)	3840.0	0.28	205.3	4.1
am	30	33	2.84	1.92	89.0	(2578, 1117)	3840.0	0.30	5064.8	4.9
am	30	35	2.79	1.90	89.0	(2578, 1117)	3840.0	0.30	4820.0	4.5
an	30	33	2.31	1.67	83.0	(1305, 1336)	3840.0	0.30	333.8	4.0
an	30	35	2.28	1.65	83.0	(1305, 1336)	3840.0	0.30	312.7	3.7
ao	0	33	2.28	1.58	−86.0	(2481, 897)	3839.0	0.28	320.8	5.1
ao	0	35	2.25	1.56	−86.0	(2481, 897)	3839.0	0.28	308.6	4.7
ap	0	33	1.88	1.53	79.0	(1314, 1347)	3836.0	0.30	469.7	3.5
ap	0	35	1.86	1.51	79.0	(1314, 1347)	3836.0	0.30	452.2	3.2
aq	0	33	1.62	1.34	−78.0	(1785, 1787)	3840.0	0.22	370.2	3.8
aq	0	35	1.60	1.32	−78.0	(1785, 1787)	3840.0	0.22	349.1	3.5
ar	40	33	2.13	2.11	85.0	(1355, 1401)	3840.0	0.29	348.7	4.2
ar	40	35	2.10	2.08	85.0	(1355, 1401)	3840.0	0.29	336.9	3.9
as	0	33	1.77	1.23	−69.0	(1965, 2020)	3837.0	0.20	308.4	4.1
as	0	35	1.75	1.21	−69.0	(1965, 2020)	3837.0	0.20	296.6	3.7
b	40	33	1.57	1.55	87.0	(1872, 1925)	3813.0	0.21	2100.5	3.2
b	40	35	1.53	1.52	87.0	(1872, 1925)	3813.0	0.21	2043.2	2.9
c	0	33	2.53	1.74	85.0	(1404, 1436)	3839.0	0.28	329.7	4.4
c	0	35	2.50	1.72	85.0	(1404, 1436)	3839.0	0.28	308.9	4.1
d	30	33	1.72	1.39	−60.0	(2022, 1556)	3839.0	0.23	156.4	4.1
d	30	35	1.69	1.37	−60.0	(2022, 1556)	3839.0	0.23	145.1	3.8
e	−30	33	2.19	1.50	83.0	(1410, 1446)	3839.0	0.28	273.6	4.6
e	−30	35	2.14	1.48	83.0	(1410, 1446)	3839.0	0.28	260.0	4.3
f	0	33	2.20	1.32	87.0	(1750, 1442)	3840.0	0.28	353.3	4.5
f	0	35	2.18	1.30	87.0	(1750, 1442)	3840.0	0.28	341.0	4.2
g	30	33	1.72	1.35	−85.0	(1572, 1619)	3840.0	0.25	198.8	4.1
g	30	35	1.68	1.32	−85.0	(1572, 1619)	3840.0	0.25	187.0	3.8
h	0	33	1.46	1.13	−78.0	(1951, 2083)	3840.0	0.21	173.2	3.9
h	0	35	1.42	1.10	−78.0	(1951, 2083)	3840.0	0.21	160.9	3.6
i	30	33	1.47	1.27	−59.0	(1646, 1613)	3832.0	0.25	260.0	3.5
i	30	35	1.43	1.23	−59.0	(1646, 1613)	3832.0	0.25	243.5	3.2
j	30	33	2.21	1.26	−87.0	(1446, 1485)	3819.0	0.27	317.1	4.6
j	30	35	2.17	1.24	−87.0	(1446, 1485)	3819.0	0.27	301.0	4.3
k	30	33	1.63	1.01	−75.0	(2174, 2167)	3832.0	0.18	140.8	4.3
k	30	35	1.60	0.99	−75.0	(2174, 2167)	3832.0	0.18	130.7	4.0
l	0	33	1.64	1.52	−51.0	(2383, 1497)	3840.0	0.26	851.0	4.1
l	0	35	1.61	1.50	−51.0	(2383, 1497)	3840.0	0.26	823.6	3.8
m	30	33	2.22	1.85	81.0	(1345, 1356)	3840.0	0.29	2975.0	3.5

Downloaded from academic.oup.com/mnras/article/552/2/stag253/8875762 by Liverpool John Moores University user on 02 November 2026

Table C1 – *continued*

Field	V_{off} (km s^{-1})	SPW_{12m}	B_{maj} ($''$)	B_{min} ($''$)	BPA (deg)	Image size (pix)	No. channels	Pixel size ($''$)	S_{peak} (mJy beam^{-1})	σ_{MAD} (mJy beam^{-1})
m	30	35	2.18	1.82	81.0	(1345, 1356)	3840.0	0.29	2850.0	3.2
n	30	33	2.62	1.28	75.0	(1366, 1823)	3840.0	0.19	231.5	5.3
n	30	35	2.60	1.25	75.0	(1366, 1823)	3840.0	0.19	218.4	4.9
o	0	33	2.04	1.56	83.0	(1281, 1230)	3835.0	0.32	378.3	4.4
o	0	35	2.00	1.53	83.0	(1281, 1230)	3835.0	0.32	359.2	4.1
p	0	33	1.58	1.26	89.0	(1856, 1839)	3836.0	0.22	270.7	3.7
p	0	35	1.54	1.23	89.0	(1856, 1839)	3836.0	0.22	255.0	3.4
q	0	33	2.02	1.55	88.0	(1315, 1343)	3836.0	0.30	279.5	3.3
q	0	35	1.99	1.53	88.0	(1315, 1343)	3836.0	0.30	262.0	3.1
r	30	33	2.34	1.36	−86.0	(1535, 1395)	3840.0	0.29	344.4	4.4
r	30	35	2.30	1.33	−86.0	(1535, 1395)	3840.0	0.29	327.0	4.1
s	0	33	2.53	1.97	80.0	(1310, 1346)	3839.0	0.30	618.6	3.8
s	0	35	2.48	1.94	80.0	(1310, 1346)	3839.0	0.30	593.7	3.5
t	0	33	2.15	1.95	65.0	(1269, 1273)	3840.0	0.31	327.7	3.9
t	0	35	2.11	1.91	65.0	(1269, 1273)	3840.0	0.31	310.8	3.6
u	30	33	1.71	1.18	−67.0	(1347, 2051)	3834.0	0.19	139.5	4.5
u	30	35	1.68	1.15	−67.0	(1347, 2051)	3834.0	0.19	130.2	4.2
v	30	33	1.60	1.02	−79.0	(1362, 1880)	3819.0	0.19	236.6	4.2
v	30	35	1.58	1.00	−79.0	(1362, 1880)	3819.0	0.19	220.5	3.9
w	30	33	2.01	1.42	−79.0	(1474, 1399)	3819.0	0.28	199.0	3.4
w	30	35	1.98	1.39	−79.0	(1474, 1399)	3819.0	0.28	189.2	3.2
x	0	33	2.20	1.49	−86.0	(1291, 769)	3836.0	0.30	396.7	4.2
x	0	35	2.17	1.46	−86.0	(1291, 769)	3836.0	0.30	377.1	3.9
y	0	33	1.86	1.37	−85.0	(1428, 1112)	3835.0	0.27	209.9	4.3
y	0	35	1.83	1.34	−85.0	(1428, 1112)	3835.0	0.27	198.2	4.0
z	40	33	1.96	1.28	79.0	(1350, 1353)	3813.0	0.29	153.1	4.3
z	40	35	1.92	1.25	79.0	(1350, 1353)	3813.0	0.29	142.7	4.0

estimated using the peak intensity of the spectrum for each pixel.

(g) `PV_l_max.fits`: ℓ-v position–velocity map from the full-resolution cube; maximum intensity taken along Galactic latitude (b).

(h) `PV_l_mean.fits`: ℓ-v position–velocity map from the masked full-resolution cube; mean intensity taken along Galactic latitude (b)

(i) `PV_b_max.fits`: b-v position–velocity map from the full-resolution cube; maximum intensity taken along Galactic longitude (ℓ).

(j) `PV_b_mean.fits`: b-v position–velocity map from the full-resolution cube; mean intensity taken along Galactic longitude (ℓ).

[1]*National Astronomical Observatory of Japan, 2-21-1 Osawa, Mitaka, Tokyo 181-8588, Japan*
[2]*UK ALMA Regional Centre Node, Jodrell Bank Centre for Astrophysics, The University of Manchester, Manchester M13 9PL, UK*
[3]*Department of Astronomy, University of Florida, PO Box 112055, Gainesville, FL 32611, USA*
[4]*European Southern Observatory (ESO), Karl-Schwarzschild-Straße 2, D-85748 Garching, Germany*
[5]*Shanghai Astronomical Observatory, Chinese Academy of Sciences, 80 Nandan Road, Shanghai 200030, P. R. China*
[6]*State Key Laboratory of Radio Astronomy and Technology, A20 Datun Road, Chaoyang District, Beijing 100101, P. R. China*
[7]*Institut de Ciències de l'Espai (ICE), CSIC, Campus UAB, Carrer de Can Magrans s/n, E-08193, Bellaterra, Barcelona, Spain*
[8]*Institut d'Estudis Espacials de Catalunya (IEEC), E-08860, Castelldefels, Barcelona, Spain*
[9]*Department of Astronomy, University of Maryland, College Park, MD 20742-2421, USA*
[10]*Max-Planck-Institut für extraterrestrische Physik, Gießenbachstraße 1, D-85748 Garching bei München, Germany*
[11]*Department of Physics and Astronomy, University of Kansas, 1251 Wescoe Hall Drive, Lawrence, KS 66045, USA*
[12]*Astrophysics Research Institute, Liverpool John Moores University, 146 Brownlow Hill, Liverpool L3 5RF, UK*
[13]*Max Planck Institute for Astronomy, Königstuhl 17, D-69117 Heidelberg, Germany*
[14]*Astronomisches Rechen-Institut, Zentrum für Astronomie der Universität Heidelberg, Mönchhofstraße 12-14, D-69120 Heidelberg, Germany*
[15]*Cosmic Origins Of Life (COOL) Research DAO*
[16]*European Southern Observatory, Alonso de Córdova, 3107, Vitacura, Santiago 763-0355, Chile*
[17]*Joint ALMA Observatory, Alonso de Córdova, 3107, Vitacura, Santiago 763-0355, Chile*

Downloaded from academic.oup.com/mnras/article/552/2/stag253/8875762 by Liverpool John Moores University user on 02 November 2026

[18]*School of Astronomy and Space Science, Nanjing University, 163 Xianlin Avenue, Nanjing 210023, P. R. China*
[19]*Key Laboratory of Modern Astronomy and Astrophysics (Nanjing University), Ministry of Education, Nanjing 210023, P. R. China*
[20]*Center for Astrophysics | Harvard & Smithsonian, 60 Garden Street, Cambridge, MA 02138, USA*
[21]*Haystack Observatory, Massachusetts Institute of Technology, 99 Millstone Road, Westford, MA 01886, USA*
[22]*Center for Astrophysics and Space Astronomy, Department of Astrophysical and Planetary Sciences, University of Colorado, Boulder, CO 80389, USA*
[23]*Department of Physics, University of Connecticut, 196A Auditorium Road, Unit 3046, Storrs, CT 06269, USA*
[24]*Centro de Astrobiología (CAB), CSIC-INTA, Carretera de Ajalvir km 4, E-28850 Torrejón de Ardoz, Madrid, Spain*
[25]*Academia Sinica Institute of Astronomy and Astrophysics, Astronomy-Mathematics Building, AS/NTU No.1, Sec. 4, Roosevelt Rd, Taipei 10617, Taiwan*
[26]*Space, Earth and Environment Department, Chalmers University of Technology, SE-412 96 Gothenburg, Sweden*
[27]*Como Lake centre for AstroPhysics (CLAP), DiSAT, Università dell'Insubria, via Valleggio 11, 22100 Como, Italy*
[28]*Institute of Physics, Laboratory for Galaxy Evolution and Spectral Modelling, EPFL, Observatoire de Sauverny, Chemin Pegasi 51, CH-1290 Versoix, Switzerland*
[29]*Observatorio Astronómico de Quito, Observatorio Astronómico Nacional, Escuela Politécnica Nacional, 170403 Quito, Ecuador*
[30]*INAF Arcetri Astrophysical Observatory, Largo Enrico Fermi 5, Firenze 50125, Italy*
[31]*Jodrell Bank Centre for Astrophysics, The University of Manchester, Manchester M13 9PL, UK*
[32]*National Radio Astronomy Observatory, 520 Edgemont Road, Charlottesville, VA 22903, USA*
[33]*Universität Heidelberg, Zentrum für Astronomie, Institut für Theoretische Astrophysik, Albert-Ueberle-Str 2, D-69120 Heidelberg, Germany*
[34]*Research School of Astronomy and Astrophysics, Australian National University, Canberra, ACT 2611, Australia*
[35]*Instituto de Astrofísica de Andalucía, CSIC, Glorieta de la Astronomía s/n, E-18008 Granada, Spain*
[36]*Instituto de Astronomía, Universidad Católica del Norte, Av. Angamos 0610, Antofagasta, Chile*
[37]*Chinese Academy of Sciences South America Center for Astronomy, National Astronomical Observatories, CAS, Beijing 100101, P. R. China*
[38]*Institute for Advanced Study, 1 Einstein Drive, Princeton, NJ 08540, USA*
[39]*Department of Physics and Astronomy, University College London, Gower Street, London WC1E 6BT, UK*
[40]*Universität Heidelberg, Interdisziplinäres Zentrum für Wissenschaftliches Rechnen, Im Neuenheimer Feld 225, D-69120 Heidelberg, Germany*
[41]*Institute for Research in Fundamental Sciences (IPM), School of Astronomy, Tehran, Iran*
[42]*Department of Physics, Villanova University, 800 E. Lancaster Ave., Villanova, PA 19085, USA*
[43]*Departamento de Astronomía, Universidad de La Serena, Raúl Bitrán 1305, La Serena, Chile*
[44]*Instituto de Física Fundamental (CSIC), Calle Serrano 121-123, E-28006, Madrid, Spain*
[45]*Green Bank Observatory, PO Box 2, Green Bank, WV 24944, USA*
[46]*Institute of Astronomy, The University of Tokyo, Mitaka, Tokyo 181-0015, Japan*
[47]*Department of Astronomy, University of Massachusetts, Amherst, MA 01003, USA*
[48]*Department of Physics, Aberystwyth University, Ceredigion, Cymru SY23 3BZ, UK*
[49]*Kavli Institute for Astronomy and Astrophysics, Peking University, Beijing 100871, P. R. China*
[50]*Department of Astronomy, School of Physics, Peking University, Beijing 100871, P. R. China*

This paper has been typeset from a TEX/LATEX file prepared by the author.

Downloaded from academic.oup.com/mnras/article/552/2/stag253/8875762 by Liverpool John Moores University user on 02 November 2026

© The Author(s) 2026.
Published by Oxford University Press on behalf of Royal Astronomical Society. This is an Open Access article distributed under the terms of the Creative Commons Attribution License (https://creativecommons.org/licenses/by/4.0/), which permits unrestricted reuse, distribution, and reproduction in any medium, provided the original work is properly cited.